Atmos. Chem. Phys., 15, 3909–3932, 2015
www.atmos-chem-phys.net/15/3909/2015/
doi:10.5194/acp-15-3909-2015

Atmospheric Chemistry and Physics
Open Access

Simulations of atmospheric OH, O_3 and NO_3 reactivities within and above the boreal forest

D. Mogensen[1,2], R. Gierens[1], J. N. Crowley[3], P. Keronen[1], S. Smolander[1,*], A. Sogachev[4], A. C. Nölscher[3], L. Zhou[1,2], M. Kulmala[1], M. J. Tang[3], J. Williams[3], and M. Boy[1,2]

[1]Department of Physics, P.O. Box 48, University of Helsinki, 00014, Finland
[2]Helsinki University Centre for Environment, P.O. Box 27, University of Helsinki, 00014, Finland
[3]Department of Atmospheric Chemistry, Max Planck Institute for Chemistry, Hahn-Meitner-Weg 1, 55128 Mainz, Germany
[4]Department of Wind Energy, Technical University of Denmark, Frederiksborgvej 399, P.O. Box 49, Building 118, 4000, Roskilde, Denmark
[*]now at: NOAA/Geophysical Fluid Dynamics Laboratory – Princeton University, Cooperative Institute for Climate Science, Princeton, NJ, USA

Correspondence to: D. Mogensen (ditte.mogensen@helsinki.fi)

Received: 5 November 2014 – Published in Atmos. Chem. Phys. Discuss.: 9 December 2014
Revised: 2 April 2015 – Accepted: 9 April 2015 – Published: 15 April 2015

Abstract. Using the 1-D atmospheric chemistry transport model SOSAA, we have investigated the atmospheric reactivity of a boreal forest ecosystem during the HUMPPA-COPEC-10 campaign (summer 2010, at SMEAR II in southern Finland). For the very first time, we present vertically resolved model simulations of the NO_3 and O_3 reactivity (R) together with the modelled and measured reactivity of OH. We find that OH is the most reactive oxidant ($R \sim 3\,s^{-1}$) followed by NO_3 ($R \sim 0.07\,s^{-1}$) and O_3 ($R \sim 2 \times 10^{-5}\,s^{-1}$). The missing OH reactivity was found to be large in accordance with measurements ($\sim 65\,\%$) as would be expected from the chemical subset described in the model. The accounted OH radical sinks were inorganic compounds ($\sim 41\,\%$, mainly due to reaction with CO), emitted monoterpenes ($\sim 14\,\%$) and oxidised biogenic volatile organic compounds ($\sim 44\,\%$). The missing reactivity is expected to be due to unknown biogenic volatile organic compounds and their photoproducts, indicating that the true main sink of OH is not expected to be inorganic compounds. The NO_3 radical was found to react mainly with primary emitted monoterpenes ($\sim 60\,\%$) and inorganic compounds ($\sim 37\,\%$, including NO_2). NO_2 is, however, only a temporary sink of NO_3 under the conditions of the campaign (with typical temperatures of 20–25 °C) and does not affect the NO_3 concentration. We discuss the difference between instantaneous and steady-state reactivity and present the first boreal forest steady-state lifetime of NO_3 (113 s). O_3 almost exclusively reacts with inorganic compounds ($\sim 91\,\%$, mainly NO, but also NO_2 during night) and less with primary emitted sesquiterpenes ($\sim 6\,\%$) and monoterpenes ($\sim 3\,\%$). When considering the concentration of the oxidants investigated, we find that OH is the oxidant that is capable of removing organic compounds at a faster rate during daytime, whereas NO_3 can remove organic molecules at a faster rate during night-time. O_3 competes with OH and NO_3 during a short period of time in the early morning (around 5 a.m. local time) and in the evening (around 7–8 p.m.). As part of this study, we developed a simple empirical parameterisation for conversion of measured spectral irradiance into actinic flux. Further, the meteorological conditions were evaluated using radiosonde observations and ground-based measurements. The overall vertical structure of the boundary layer is discussed, together with validation of the surface energy balance and turbulent fluxes. The sensible heat and momentum fluxes above the canopy were on average overestimated, while the latent heat flux was underestimated.

Published by Copernicus Publications on behalf of the European Geosciences Union.

1 Introduction

As most biogenically and anthropogenically emitted trace gases are oxidised within the Earth's boundary layer, the oxidising capacity of this layer may be considered to be approximately that of the atmosphere. The concentrations of oxidants and their reactivity towards a vast number of compounds and pollutants, together with the concentration of these pollutants, impact on the local air quality. Anthropogenic activity, resulting in increased sources of air pollution and more intense forest management (e.g. deforestation), results in changes in the composition of the atmosphere and potentially in its oxidation capacity.

The OH radical is considered the main atmospheric cleaning agent, and consequently it has received a lot of attention (e.g. Levy II, 1971; Mount and Eisele, 1992; Lelieveld et al., 2008; Mogensen et al., 2011, and references therein). Being highly reactive, OH has a short lifetime (depending on the conditions, but usually much less than 1 s; Jacob, 1999) and is capable of reacting with most functional groups. The concentration of OH was first measured in the 1970s (Wang and Davis, 1974), but even with great advances in instrument development, it is still difficult to detect such low concentrations of such a reactive compound (Mao et al., 2012; Novelli et al., 2014a, b). The measurement is therefore still associated with large uncertainties. The reactivity of OH, its summed first-order loss rate constant from the atmosphere, has been measured in both urban (e.g. Ren et al., 2003; Lou et al., 2010) and remote and forested environments (e.g. Kovacs et al., 2003; Nölscher et al., 2012a; Sinha et al., 2010). Common to most investigations, especially those in forested areas, is the large missing fraction of the OH reactivity. This means that OH is lost due to unaccounted processes that is most often attributed to unmeasured and unidentified compounds either originating from direct emission or formed via oxidation processes (e.g. Mount and Eisele, 1992; Di Carlo et al., 2004; Sinha et al., 2010).

While the OH concentration has a clear daily profile with a daytime peak due to its large photolytic source, it is absent or present at much lower concentrations during the night when other oxidants such as the NO_3 radical or O_3 play an increasingly significant role. Typical O_3 mixing ratios are in the range of tens of ppb, whereas NO_3 is rarely present at mixing ratios more than a few hundred ppt and typically less than 100 ppt. While the reactivity of NO_3 has never been directly measured (e.g. Brown et al., 2011, and references therein), some recent studies have addressed O_3 reactivity (Park et al., 2013; Matsumoto, 2014). So far no one has modelled the reactivity of either O_3 or NO_3.

After the tropical forest, the boreal forest zone and the temperate forests together represent the largest forested area worldwide (Guenther, 2013) and it produces a large number of different volatile organic compounds (VOCs). It is estimated that the boreal forest zone accounts for about 5 % of the global emission of biogenic VOCs (BVOCs) (Guenther, 2013). These VOCs can react with the above-mentioned oxidants and thereby alter the atmospheric oxidation budget and produce new products with different chemical and physical properties. These compounds often have lower vapour pressures than their parent molecule and have the potential to participate in aerosol formation and growth as well as in production of cloud condensation nuclei (CCN) and thereby affect the climate (e.g. Makkonen et al., 2012; Ehn et al., 2014).

An accurate description of vertical fluxes, and therefore validation of the overall meteorological situation, is essential to reach our main goals, which are the following:

- to evaluate model uncertainties due to the use of measured input gas concentrations.
- to create a simple empirical parameterisation for conversion of measured spectral irradiance into actinic flux in order to calculate photodissociation rates.
- to model the reactivity of OH and – for the first time – that of O_3 and NO_3 and to investigate their reactivity towards specific groups of compounds, thereby mapping the diel behaviour of their relative importance.

Our method in order to achieve these goals is a 1-D chemistry transport model so that we are also able to investigate the vertical importance of the compounds of interest. Our location of choice is the SMEAR II station, which is very well characterised and also located in the boreal forest zone.

2 The site

All compounds presented here were measured during the HUMPPA-COPEC-10 campaign (Hyytiälä United Measurement of Photochemistry and Particles – Comprehensive Organic Particle and Environmental Chemistry 2010). This extensive campaign was carried out at the SMEAR II station (Station for Measuring Ecosystem–Atmosphere Relations), Hyytiälä, southern Finland (e.g. Hari and Kulmala, 2005; Vesala et al., 1998; Kulmala et al., 2001a). The campaign took place between 12 July and 12 August 2010, and the aim of the campaign, including instrumental set-up, is provided by Williams et al. (2011). Continuous measurements (with less instrumentation than during the campaign) are carried out at the SMEAR II site.

The SMEAR II station is located in the southern boreal forest zone. The vegetation mostly consists of conifer trees, in particular Scots pine (Haapanala et al., 2007). Williams et al. (2011) describe the meteorological situation, including anthropogenic influences, during the campaign in detail; thus we only provide a short summary here: the campaign took place during an anomalously warm summer, with an average temperature of 20 °C. During the campaign, air advected to the site mostly from the SW (53.7 %) but also from the SE (20.7 %) and from the NW (10.3 %). The site was impacted by periods of advected biomass burning emissions, emissions

from urban centres in the SW and occasionally by a nearby sawmill. The periods with anthropogenic influences were not considered in this study.

3 Measured gases used as input to the model

The ambient concentrations of NO, NO_2 ($= [NO_x] - [NO]$), SO_2, O_3 and CO are continuously measured at the SMEAR II station, and their averaged daily profiles are illustrated in Fig. 1. Since their sources are mostly of anthropogenic origin, we use the concentration of these compounds as input to our model. Some model uncertainty stems from the uncertainty in the concentration of these input gases. For this reason, in Sect. 7.2, we intercompare critical trace gases from the SMEAR II site with additional campaign measurements. Since the concentration of SO_2 was only measured by one instrument, we will obviously exclude these data from the intercomparison. Below we go through the measurement details of the mentioned trace gases. All of the below-mentioned campaign-based gases were measured by researchers from the Max Planck Institute (MPI) at 24 m with an original recording interval of 1 s. The SMEAR II gases are continuously measured at several heights: 67.2, 50.4, 33.6, 16.8, 8.4 and 4.2 m above the SMEAR II mast base. The original recording interval was 1 min at 6 min time interval for each measurement height. For the later intercomparison, we chose to only focus on the averaged data from 33.6 and 16.8 m. In case of CO the measurements were performed only at 16.8 m. The campaign-based measurements were carried out on a tower approximately 30 m from the SMEAR II mast. For details on the non-SMEAR II trace gas measurements, we refer to Williams et al. (2011).

3.1 NO and NO_x measurements

The continuous SMEAR II NO and NO_x concentrations were measured with one chemiluminescence analyser (TEI 42C TL, Thermo Fisher Scientific, Waltham, MA, USA). NO_2 was measured indirectly by using a NO_2-specific photolytic converter (Blue Light Converter, Droplet Measurement Technologies, Boulder, CO, USA). The NO_2 concentration was calculated as the difference between the measured NO_x and NO concentrations. The detection limit was 0.1 ppb for NO and 0.15 ppb for NO_2. The total accuracy for NO was ± 0.05 and ± 0.09 ppb for NO_2. The effect of oxidation of NO to NO_2 by the reaction between NO and O_3 inside the sample lines was estimated to be smaller than the measurement accuracy. The concentrations of both NO and NO_2 were additionally measured specifically for this campaign by MPI using a modified commercial chemiluminescence detector (CLD 790 SR) originally manufactured by ECO Physics (Duernten, Switzerland) (Hosaynali Beygi et al., 2011). NO_2 was measured indirectly by conversion to NO using a blue light converter. The detection limits for the NO and NO_2 measurements were 10 and 80 ppt, respectively, for an integration period of 2 s. The total accuracy of the original NO data was ± 0.01 ppb, while the total accuracy of that NO_2 data was ± 0.03 ppb.

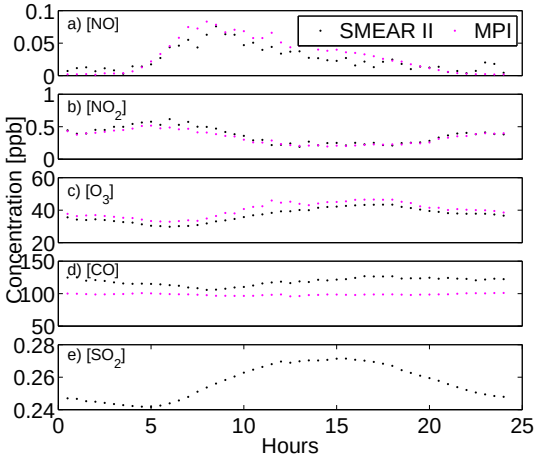

Figure 1. The daily averaged measured concentration of **(a)** NO, **(b)** NO_2, **(c)** O_3, **(d)** CO, and **(e)** SO_2 during the campaign. The SMEAR II mast data are shown in black, while the extra measurements by MPI are shown in magenta.

The high detection limit of the SMEAR II chemiluminescence analyser is a problem, since the concentrations of NO and NO_2 are generally low at our site (~ 0.02 and ~ 0.3 ppb, respectively, for this campaign). For previous studies (e.g. Mogensen et al., 2011), we have defined the concentration of both NO and NO_2 to be 5 ppt when the measured concentrations were below the detection limit. Since one of the main aims of this paper is to investigate the reactivity of NO_3, and since the concentrations of NO and NO_2 are crucial in order to obtain this, we chose to use the MPI-measured NO_x concentrations for our simulations due to the high sensitivity of the MPI instrument, unless otherwise specified. For SO_2, O_3 and CO we used the SMEAR II data.

3.2 O_3 measurements

The O_3 concentration is continuously measured at SMEAR II using one ultraviolet light absorption analyser (TEI 49C, Thermo Fisher Scientific, Waltham, MA, USA). The detection limit is 1 ppb, while the total accuracy is ± 1 ppb. The O_3 concentration was further measured for this campaign by MPI using a UV instrument, sharing the inlet line with the MPI chemiluminescence detection system (CLD) for measuring NO and NO_2. The detection limit was ~ 1 ppb, while the total accuracy was ± 4 ppb. Both instruments were calibrated against ozone standards during (MPI instrument) or after (SMEAR II instrument) the campaign.

3.3 CO measurements

The CO concentration was measured on the SMEAR II mast with one infrared light absorption analyser (API 300EU, Teledyne Monitor Labs, Englewood, CO, USA). The detection limit was 50 ppb, while the total accuracy was ±25 ppb. Additionally, the CO concentration was also measured during the campaign by MPI using a commercial vacuum UV resonance fluorescence CO instrument (AeroLaser GmbH, Garmisch-Partenkirchen, Germany). The detection limit was ∼ 1 ppb, while the total accuracy was ±10 ppb.

3.4 SO_2 measurements

The SO_2 concentration was measured on the SMEAR II mast with one fluorescence analyser (TEI 43 CTL, Thermo Fisher Scientific, Waltham, MA, USA). The detection limit was 0.1 ppb and the total accuracy was ±0.05 ppb. The measurement principle is described in Rosman et al. (2001) though the same analyser is no longer in use at the site.

4 Measurements during the HUMPPA-COPEC-10 campaign

4.1 Meteorological sondes

Ouwersloot et al. (2012) studied the convective boundary layer during the HUMPPA-COPEC-10 campaign and describe in detail the radiosondes measurements. In short, during the entire campaign, 175 GRAW DFM-06 radiosondes were launched at a distance of ∼ 300 m from the SMEAR II station. Five radiosondes were launched every day except for 4 days when the measurements were made every second hour. The radiosondes operated on-line and contained temperature and humidity sensors together with a GPS. The GPS was accurate within 10 m, the temperature sensor within 0.2 °C, while the humidity sensor measured with an accuracy of 2 %.

4.2 Photolysis rates

Filter radiometers (from Forschungszentrum Jülich and the Max Planck Institute for Chemistry) were used to measure the atmospheric photolysis frequencies $J(NO_2)$ ($NO_2 + h\nu(\lambda \leq 420\,nm) \rightarrow O(^3P) + NO$) and $J(O^1D)$($O_3 + h\nu(\lambda \leq 340\,nm) \rightarrow O(^1D) + O_2$) (Bohn et al., 2008). It is very difficult to estimate the measurement uncertainty in photolysis rates measured by filter radiometers; however, Bohn et al. (2008) report that when intercomparing $J(NO_2)$, the results differ by 5–8 % and the instrument correlation for $J(O^1D)$ is poorer with larger scatter at large solar zenith angles. Since the filter radiometers were compared with a reference spectroradiometer instrument before and after the campaign, and since recent technical developments have improved the measurement of $J(O^1D)$, we expect that the uncertainties in our measured photolysis rates are less than what is reported by Bohn et al. (2008) (after personal communication with Birger Bohn, 2014). Both rates were measured at ground level in a clearing partly blocked by trees, and above the canopy at 24 m, with a full view of the upper hemisphere.

4.3 Measurements of OH reactivity

The total OH reactivity was measured using the comparative reactivity method (CRM, from the Max Planck Institute for Chemistry) (Sinha et al., 2008) at 18 and 24 m. We refer to Nölscher et al. (2012a) and Nölscher et al. (2012b) for details on the set-up. The instrument operated with a detection limit of 3–4 s^{-1} with respect to the baseline noise (2σ). The overall measurement uncertainty is estimated to be 16 % based on errors in the detector (5 %), rate coefficient (14 %), gas standard (5 %) and dilution (2 %). The uncertainty is calculated based on propagation of uncertainty.

4.4 Measurement of NO_3 and N_2O_5

NO_3 (and N_2O_5) mixing ratios were measured using a two-channel, cavity ring-down system, which has recently been described in detail (Crowley et al., 2010b; Schuster et al., 2009). The reported detection limit for NO_3 is 1–2 ppt in 3 s integration. By averaging data over several minutes, this is reduced significantly (to < 1 ppt) at which point fluctuations in the zero measurement (obtained by adding NO) prevent further reduction of the detection limit. The total uncertainty is reported as 15 % (at least 2 ppt) and 15 % (at least 3 ppt) for NO_3 and N_2O_5 respectively (Crowley et al., 2010b). The instrument for measuring NO_3 was located on the top of the 24 m tower, approximately 1 m from (and at the same height as) the inlets of the MPI-CLD instrument measuring NO and NO_2.

5 The SOSAA model

We used the 1-D chemistry transport model SOSAA (model to Simulate Organic vapours, Sulphuric Acid and Aerosols) for model simulations. The structure and content of SOSAA have been described in detail in several other papers (e.g. Boy et al., 2011; Mogensen et al., 2011; Boy et al., 2013; Smolander et al., 2014; Zhou et al., 2014; Mogensen et al., 2015). We provide a recap here together with included updates.

SOSAA is programmed in Fortran 90 and consists of modules for (1) planetary boundary layer meteorology and turbulent mixing, (2) biogenic tree and soil emission of volatile organic compounds, (3) radiative transfer and gas-phase chemical reactions and (4) aerosol dynamics. The aerosol module is an extension to the original model SOSA (model to Simulate Organic vapours and Sulphuric Acid), and it is described in the paper by Zhou et al. (2014). Since we are not simulating the aerosol phase in this paper, we will not go through this particular part of SOSAA. The structure of SOSAA is

illustrated in Fig. 2. The internal time step for the meteorological module is 10 s, while the time step for the additional modules is 60 s. The chemistry and aerosol modules utilises parallel computing.

5.1 Meteorology and vertical mixing

The meteorological module in SOSAA is based on the 1-D version of SCADIS (Scalar Distribution) (Boy et al., 2011, and references therein). It consists of prognostic equations for temperature, horizontal wind speed, humidity, turbulent kinetic energy (TKE) and the specific dissipation rate of TKE (ω). Since the representation of a three-dimensional flow in a one-dimensional model is limited, nudging (Anthes, 1974) of temperature, horizontal wind speed and humidity was done in order to represent effects from local to synoptic-scale flow patterns. Measurement data from the SMEAR II station and a nudging factor of 0.01 were used. In order to solve turbulent fluxes, a TKE-ω type closure scheme, also called two-equation closure, was applied (Sogachev, 2009). In this study we used a domain reaching from the surface to 3000 m, with 51 logarithmically distributed vertical layers. The grid density was highest close to the surface and sparser higher up with 19 of the layers being inside the canopy in the lowest 18 m.

Interactions between the atmosphere and vegetative canopy are described in detail – including plant drag, exchange of heat and moisture and radiative processes (reflection, penetration, absorption and emission for three wavelength bands) at each modelled canopy layer. For calculating sensible and latent heat fluxes and for solving the energy balance closure, prognostic equations for soil moisture and temperature are included in the model.

Several updates were made in order to improve the model performance. The changes made in the turbulent closure scheme and parameterisations for latent and sensible heat fluxes are described by Sogachev et al. (2012). According to Boy et al. (2011), simulation of thermal radiation from the atmosphere was not successful due to missing cloud cover records. To overcome this issue, radiation data from ERA-Interim reanalysis (Dee et al., 2011) provided by the European Centre for Medium-Range Weather Forecasts (ECMWF) were used as model input. To further improve the accuracy of the surface energy balance, the heat flux and storage into the soil was taken from observations made at SMEAR II, when available. In case of measurement gaps longer than 4 h, the original parameterisation (Sogachev et al., 2002) was used to estimate the flux, with the addition of using measured soil temperature as input for the deepest soil level (40 cm below the surface). Furthermore, measured soil water content in the humus layer was used as the water content of soil layer 1 (Sogachev et al., 2002) and hence the original prognostic equations for soil moisture were neglected.

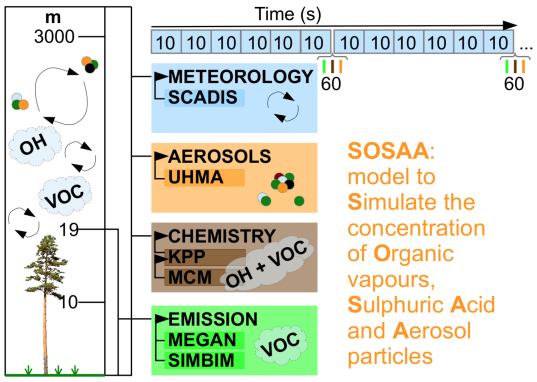

Figure 2. The model structure of SOSAA: SCADIS describes the meteorological evolution of the vertical domain, followed by either MEGAN or SIMBIM that provide emissions of VOCs from the individual levels of the canopy. Chemical reactions are chosen from the MCM and processed by the KPP, whereafter aerosol dynamical processes are calculated by the University of Helsinki Multicomponent Aerosol model.

Upper border boundary condition values for wind speed, temperature and its gradient, and humidity are from Era-Interim reanalysis by ECMWF. These data were used instead of the soundings for two reasons. Firstly, the data are available at any location and at a fixed resolution for any day of the year. Secondly, soundings are by nature snapshots of the vertical column, while the Era-Interim data aim to provide an average value of the grid cell presented. The Era-Interim reanalysis data are available with 6 and 3 h (temperature, humidity, horizontal wind speed and thermal radiation, respectively) temporal resolution. Direct and diffuse global radiation measured at SMEAR II were used as input for the meteorological scheme to improve the accuracy of the energy balance closure. All input data used in the model are linearly interpolated between data points to every model time step.

5.2 VOC emission from trees

SOSAA includes several modules for calculation of the tree emission of VOCs. For the simulations presented in this paper, we have used a modification of MEGAN (Model of Emissions of Gases and Aerosols from Nature) version 2.04 (Guenther et al., 2006). The tree emissions of VOCs are calculated using the canopy structure, VOC-specific standard emission potentials (SEPs) and the emission activity of the trees. The dominant tree species is Scots pine, the canopy height is ~ 18.5 m, while the canopy depth is ~ 9 m with a total leaf area index (LAI) of 5.8 (Ilvesniemi et al., 2009; Palmroth and Hari, 2001) and a biomass of 0.0538 g cm^{-2}. The leaf area density distribution is based on observations at the site. The above-ground understorey vegetation consists of ~ 60 % vascular plants (mostly shrubs) and ~ 40 % mosses (Ilvesniemi et al., 2009), but we only considered BVOC emission from the Scots pine. We included SEPs of iso-

prene, 2-methyl-3-buten-2-ol, monoterpenes and sesquiterpenes measured at the site (Mogensen et al., 2015; Bäck et al., 2012; Hakola et al., 2006; Simpson et al., 1999). The monoterpenes included are α-pinene, Δ^3-carene, β-pinene, limonene, cineol and a lumped group of minor monoterpenes, and their emission distribution is based on the average chemotype presented in Bäck et al. (2012). Lastly, the emission activity depends on the LAI and is furthermore controlled by meteorological factors (radiation and temperature). For explicit and recent updates in our version of MEGAN, we refer to Mogensen et al. (2015). The calculated concentration of a specific BVOC at each model level depends on the predicted emission of that compound in that specific level, the concentration of reactants in the same level and the transport to/from the level.

5.3 Radiative transfer

5.3.1 Irradiance and actinic flux

As mentioned in Sect. 4.2, the photolysis rates $J(NO_2)$ and $J(O^1D)$ were measured during this campaign above the canopy and at ground level in a clearing. Further, the spectral irradiance was also measured. In order to calculate all relevant photolysis rates (listed in Sect. 5.3.2) at all simulated levels inside the canopy, we needed to convert the spectral irradiance into actinic flux.

In order to calculate photodissociation of any compound, the following information is crucial: (1) the compound-specific wavelength- and temperature-dependent absorption cross section and quantum yield as well as (2) the wavelength- and altitude-dependent solar actinic flux. Absorption cross sections and quantum yields are measurable laboratory quantities. Measurements of solar actinic fluxes are rare and difficult; instead the spectral irradiance is more commonly obtained, which is also the situation at the SMEAR II station. Here the irradiance is measured by a Bentham DM150 double monochromator (Boy and Kulmala, 2002). The difference in irradiance and actinic flux arises because the irradiance describes the flow of radiant energy through the atmosphere, while the actinic flux concerns probability of an encounter between a photon and a molecule (Madronich, 1987). Many attempts have been made to develop parameterisations to convert measured irradiance into actinic flux (e.g. Kazadzis et al., 2000; Webb et al., 2002; Kylling et al., 2003; Kazadzis et al., 2004); however, most often the ratio between diffuse and total downwelling irradiance or the ratio of direct to global irradiance is needed. Those ratios are often not measured, and it can be difficult to estimate since it depends on the aerosol load, potential clouds, surface albedo, solar zenith angle and wavelength, which are not all available. We used the radiative transfer tool "uvspec" version 1.7 from the libRadtran package (http://www.libradtran.org/doku.php) to calculate the ratio between diffuse and total downwelling irradiance (E_0/E) and Eq. (7) in Kylling et al. (2003) in order to convert our measured irradiance into actinic flux. uvspec provides many options to specify the atmosphere. However, we are lacking most of this information; thus we had to estimate the different parameters. Unfortunately this parameterisation (due to lack of input) was not capable of reproducing the measured photolysis rates. Instead a simpler empirical approach was taken. Firstly we modelled the two photolysis rates $J(NO_2)$ and $J(O^1D)$ assuming that the measured irradiance equaled the actinic flux. Then the two ratios between the measured and modelled photolysis rates were calculated as a function of solar zenith angle for the entire campaign period, and the median was taken for every integer of the solar zenith angle. If the solar zenith angle is zero, then our ratio was also defined as zero. Based on the quantum yield, cross section and irradiance, we estimated that the peak of photolysis of NO_2 was found at 390 nm and at 305 nm in the case of photolysis of O_3 to form O^1D. Therefore the two calculated ratios were allocated to the wavelengths of 305 and 390 nm. We then linearly interpolated the ratios between 305 and 390 for every solar zenith angle. In the interval 280–305 nm we assume a similar ratio as for 305 nm, and in the interval 390–700 nm we assumed the same ratio as for 390 . In the SOSAA model, we then multiplied this wavelength- and solar-zenith-angle-dependent ratio by the wavelength- and solar-zenith-angle-dependent measured spectral irradiance and obtained new photolysis rates. Though the ratio in theory is expected to be greater than unity (since irradiance refers to radiation weighted with the cosine of the incidence angle, and actinic flux is equally weighted from every direction), we observe that the ratio is only larger than unity at 390 nm, but not at 305 nm. In order to match the measured photolysis rates of NO_2, we need to multiply the measured spectral irradiance by a value of $\sim$ 1.7–2.8, but in case of obtaining reasonable photolysis rates of O^1D, we need to multiply the irradiance by a factor of $\sim$ 0.5–0.7 (this shows a strong decrease with increasing solar zenith angle).

For comparison, we also calculated photolysis rates using the Tropospheric Ultraviolet and Visible (TUV) Radiation Model v5.0 (http://cprm.acd.ucar.edu/Models/TUV/). This model calculates the altitude-dependent clear-sky (there is also an option to add clouds) actinic flux for any given latitude, longitude and time. If the clear-sky TUV is used, this would result in maximum photolysis rates. We calculated the radiation with a four-stream discrete and used the defin2 model input with SMEAR II location, but otherwise only default values were used.

5.3.2 Photolysis reactions

We have included all available photolysis reactions from MCM (Master Chemical Mechanism) v3.2 (which are originally mostly from Atkinson et al., 2004). More information on MCM is found in Sect. 5.4. Additionally we added the photodissociation of HO_2NO_2 (via one channel to form HO_2

and NO_2 and via the other channel to form OH and NO_3) and of N_2O_5 (via one channel to form NO_2 and NO_3 and via the other channel to form NO_3, NO and O) (Atkinson et al., 2004).

5.4 Gas-phase chemical reactions

The measured trace gas mixing ratios which were used to constrain the model are described in Sect. 3. Further, we use a constant mixing ratio of H_2 (0.5 ppm) and CH_4 (1.8 ppm). The concentrations of all other compounds are calculated based on their emission and their chemical production and/or degradation according to the chemical mechanistic information from MCM v3.2 (Jenkin et al., 1997; Saunders et al., 2003; Jenkin et al., 2012) via the following website: http://mcm.leeds.ac.uk/MCM. The chemical mechanisms from MCM are processed using KPP – Kinetic PreProcessor (Damian et al., 2002) to produce Fortran90 files containing the concentration time derivative functions and their Jacobian for all included compounds, together with the chemical solver LSODE (Radhakrishnan and Hindmarsh, 1993). We have included the necessary inorganic MCM reactions together with the full MCM chemical degradation paths for methane, isoprene, 2-methyl-3-buten-2-ol, α-pinene, β-pinene, limonene and β-caryophyllene. For other emitted organic compounds where no MCM chemistry path is available, we have included their first-order oxidation reactions with OH, O_3 and NO_3. Those compounds include the following: cineole, Δ^3-carene, "other monoterpenes" than those mentioned here, farnesene and "other sesquiterpenes" than those mentioned here (Atkinson, 1994). For the reactions of the stabilised Criegee intermediates (sCIs), we diverted from the MCM and instead used newer obtained reaction rates. For the sCIs from α-pinene, β-pinene and limonene, we have used the rates from Mauldin III et al. (2012) similarly to "Scenario C" in Boy et al. (2013). For the sCIs from isoprene, we used the rates from Welz et al. (2012) as done in "Scenario D" in Boy et al. (2013). Only biogenic VOC emissions are estimated; thus we do not include the chemistry mechanisms for anthropogenic VOCs. The abundance of anthropogenic VOCs in SMEAR II is generally low, and we do currently not have a way to predict their concentration. Sulfuric acid and nitric acid are removed from the gas phase depending on the condensation sink. The condensation sink is based on measurements and calculated according to Kulmala et al. (2001b).

5.5 Instantaneous and steady-state oxidant reactivity

When considering or calculating the reactivity, loss rate, of, for example, OH or NO_3, we need to differentiate between *instantaneous reactivity* (R_{inst}) and the reactivity that defines the *turnover lifetime* of the radical out of steady state (R_{ss}). The instantaneous OH reactivity has previously been modelled using SOSAA, and we refer to Mogensen et al. (2011) for how this was explicitly done. Since OH is not the only important atmospheric oxidant, we extended our calculations to also cover the reactivities of O_3 and NO_3 (we will denote them O_3 reactivity and NO_3 reactivity, respectively). The reactivity related to a single reaction is calculated by multiplying the reaction rate coefficient (between either of the oxidants and the reactant) by the concentration of the reactant. The total instantaneous reactivity is then the sum of all these terms, which means all sink reactions have been taken into account regardless of whether these reactions lead to reformation of the radical or not:

$$R_{\mathrm{OX,inst}} = \sum_{\mathrm{Reactions}} k_{\mathrm{OX+Y}} \times [\mathrm{Y}]. \quad \text{(R1)}$$

$R_{\mathrm{OX,inst}}$ is the total instantaneous reactivity of the oxidant (where OX is either OH, O_3 or NO_3), and $k_{\mathrm{OX+Y}}$ is the bimolecular reaction rate coefficient for the chemical reaction between the oxidant and the chemical species Y, where the concentration of Y is given by [Y]. Instead of only considering the total instantaneous reactivities, we also investigated the reactivities with respect to certain groups of compounds (e.g. inorganic compounds, isoprene, monoterpenes and the sesquiterpenes). In our definition of these reactivities, also the reactivities due to reactions between the oxidants and secondary or higher-order reaction products arising from a primary reaction are included. The OH recycling mechanisms available in MCM version 3.2 are taken into account. For NO_3 we also report the instantaneous reactivity, which is why its reaction with NO_2 (forming N_2O_5) is included as a loss term even though NO_3 is reformed from thermal decomposition of N_2O_5 (see below). This is then entirely analogous to measured and reported instantaneous reactivity of OH.

The inverse of the instantaneous reactivity is the instantaneous lifetime (τ_{inst}):

$$R_{\mathrm{OX,inst}} = \frac{1}{\tau_{\mathrm{inst}}}. \quad \text{(R2)}$$

This instantaneous lifetime is distinct from turnover lifetimes (τ_{ss}) derived from steady-state analysis of, for example, measured radical concentrations ([radical]) and known production (P_{net}) terms:

$$R_{\mathrm{ss}} = \frac{P_{\mathrm{net}}}{[\mathrm{radical}]} = \frac{1}{\tau_{\mathrm{ss}}}. \quad \text{(R3)}$$

As the steady-state lifetime deals with net production and loss terms, it takes into account the reformation of, for example, OH or NO_3 other than in the primary production term(s). We illustrate this below for NO_3. The formation and loss of NO_3 in the atmosphere can be described by the following set of Reactions (R4)–(R8) with rate coefficients k_4 to k_8.

$$NO_2 + O_3 \rightarrow NO_3 + O_2, k_4 \quad \text{(R4)}$$

$$NO_3 + NO_2 + M \rightarrow N_2O_5 + M, k_5 \quad \text{(R5)}$$

$$N_2O_5 + M \rightarrow NO_2 + NO_3 + M, k_6 \quad \text{(R6)}$$

$$N_2O_5 \rightarrow \text{products}, k_7 \quad \text{(R7)}$$

$$NO_3 \rightarrow \text{products}, k_8 \quad \text{(R8)}$$

Reaction (R7) represents loss of N_2O_5 to aerosol and surfaces, and Reaction (R8) represents all gas-phase reactions of NO_3 (mainly with NO and hydrocarbons). We assume that the gas-phase loss of N_2O_5 via reaction with water vapour is not significant (IUPAC, 2014; Brown et al., 2006; Crowley et al., 2010b). Considering Reactions (R4) to (R8), the concentration of N_2O_5 in steady state ($[N_2O_5]_{ss}$) is given by

$$[N_2O_5]_{ss} = \frac{k_5[NO_2][NO_3]}{k_6 + k_7}, \quad \text{(R9)}$$

whilst that of NO_3, ($[NO_3]_{ss}$), is given by

$$[NO_3]_{ss} = \frac{k_4[NO_2][O_3]}{k_5[NO_2] - \frac{k_5 k_6[NO_2]}{k_7 + k_6} + k_8}. \quad \text{(R10)}$$

To simplify, we consider two extreme cases. In case 1, the fate of N_2O_5 is dominated by thermal dissociation to NO_2 and NO_3 ($k_6 \gg k_7$). In case 2, the fate of N_2O_5 is dominated by heterogeneous loss to particles/surfaces ($k_7 \gg k_6$). In case 1, the reaction of NO_2 with NO_3 does not represent a sink of NO_3 as the N_2O_5 product regenerates NO_3. The steady-state concentration of NO_3 is then

$$[NO_3]_{ss} = \frac{k_4[NO_2][O_3]}{k_8}. \quad \text{(R11)}$$

As discussed above, the numerator is the NO_3 production term so that the steady-state reactivity (denominator) is given simply as k_8. In case 2 the reaction of NO_3 with NO_2 is a sink of NO_3 as the reformation of NO_3 via the thermal dissociation of N_2O_5 is insignificant. Here, the steady-state concentration of NO_3 is given by

$$[NO_3]_{ss} = \frac{k_4[NO_2][O_3]}{k_5[NO_2] + k_8} \quad \text{(R12)}$$

so that the steady-state reactivity is given by $k_5[NO_2] + k_8$, which is the same as the instantaneous reactivity. We can now evaluate which of these two scenarios more closely represents the situation during the HUMPPA-COPEC-10 campaign. We note that the N_2O_5 thermal dissociation rate constant (k_6) is highly temperature dependent, and for typical HUMPPA conditions (20–25 °C) it is $\sim 4 \times 10^{-2}\,s^{-1}$. In contrast, k_7 is defined by a combination of available aerosol surface area and reactivity and dry deposition and is given by $k_7 \sim 0.25\gamma\widetilde{c}A + k_{dd}$, where A is the aerosol surface area, γ the uptake coefficient and $\widetilde{c}$ the mean molecular velocity (Crowley et al., 2010a), while k_{dd} is the loss frequency of N_2O_5 due to dry deposition. Combining a typical value of $A = 1 \times 10^{-7}\,cm^2\,cm^{-3}$ at SMEAR II with $\gamma = 0.03$–0.001 (Bertram et al., 2009; Chang et al., 2011) with $\widetilde{c} = 24\,000\,cm\,s^{-1}$, and an upper limit of $3 \times 10^{-5}\ s^{-1}$ for the loss frequency of N_2O_5 due to dry deposition in a neutrally stratified nocturnal boundary layer of 100 m height (Geyer et al., 2001), we derive $k_7 \sim 1 \times 10^{-4}$–$5 \times 10^{-5}\,s^{-1}$. This implies that for the warm temperatures encountered during HUMPPA, case 1 is dominant, and the instantaneous reactivity, which includes a contribution from reaction with NO_2, will be larger than the steady-state reactivity. Similar arguments apply when considering the reactivity of OH. In this case, due to the many reactions of OH which lead to its reformation on relatively short timescales, the difference between instantaneous and steady-state lifetimes will be greater. Examples are the reaction of OH with CO and hydrocarbons in the presence of NO which reform OH (via HO_2) on timescales of a few minutes. In the rest of the paper, we will refer to the instantaneous reactivity as just "reactivity" but specify when using steady-state reactivity.

Computing oxidant reactivity

In order to model the reactivity of the three oxidants, we wrote a script in the Python programming language (using the pattern matching operations in the regular expressions module) in order to find the bimolecular reactions involving OH, NO_3 and O_3 from the MCM files. The reactions were postprocessed into additional "bookkeeping reactions", whereby we could calculate the time evolution of the instantaneous reactivities along with the time evolution of the real chemical concentrations.

6 Model validation

For the traces gases used to constrain the model, the photolysis rates and the OH reactivity, the following uncertainty and error analysis is provided: SDs, the Pearson's product-moment correlation coefficient which describes colinearity between the measured and modelled parameters and the coefficient of determination which describes the proportion of the total variance explained by the model. We also provide the slope and the intercept of the linear least-square regression, where the slope will be one and the intercept zero, if the model predicts the measured results perfectly. Also provided is the mean square error (MSE) together with the total root mean square error (RMSE) that shows the actual error, since it has the same unit as the parameter investigated, and the systematic (linear error) component, which is the square of the sum of the additive and proportional components of the mean square error together with their interdependence. The unsystematic (i.e. nonlinear error) RMSE is also given. For comparison, bias, which gives the difference between the mean of the measured and the mean of the modelled variable,

is also included. Lastly we also included the "index of agreement" (d), which reflects the degree to which the measured parameter is accurately modelled and is error free. If d is one, the model and measured values are identical; however, if d is zero, the model cannot represent the measured value at all. For a detailed description on the included validation methods, we refer to Willmott (1981).

7 Results and discussion

In order to provide results for the unperturbed boreal forest, we filtered out the measurement periods during which pollution occurred. The pollution originated from either biomass burning, anthropogenic influence or from the local sawmill. We refer to Williams et al. (2011) for the specific times and details on classification of the pollution events.

7.1 The meteorological situation

The validation of the meteorological scheme is done firstly for the full vertical domain using data obtained by the radiosonde measurements and secondly in the surface layer using the continuous measurements conducted at the SMEAR II station. The polluted periods are also included in this analysis, since it will not affect the meteorology.

7.1.1 Vertical profiles

Examples of vertical profiles of wind speed, potential temperature and absolute humidity on two occasions, 12 p.m. on 12 July and 3 a.m. on the 11 July, are shown in Fig. 3. The model values shown are 30 min averages during which the radiosondes were started. Data from the SMEAR II tower are included in order to supplement the radiosonde data in the lowest 100 m. These data are also averaged for 30 min, and one should keep in mind that they were obtained with different instruments than those used on the sondes. The upper panel is from 12 p.m.; the mixed layer has been developing throughout the morning and has reached 1100–1300 m, which is observed both in the model and by the radiosonde. The model underestimates the depth of the mixed layer, determined here as the depth where the gradient of potential temperature is approximately zero or negative. In the model the height of the atmospheric boundary layer (ABL) is defined as the lowest model level where the Richardson number (Ri) exceeds the limit of 0.25. The figure suggests that this parameterisation is able to set the top of the boundary layer close to the height assessed by the potential temperature and wind speed profiles. The underestimation of the height of the mixed layer could be caused by too strong temperature gradients above the boundary layer (clearly visible in the example chosen), which would limit the growth of the mixed layer. However, since the focus in this study is on chemistry close to the surface, we found the agreement between the simulations and observations satisfactory as well as the possibilities

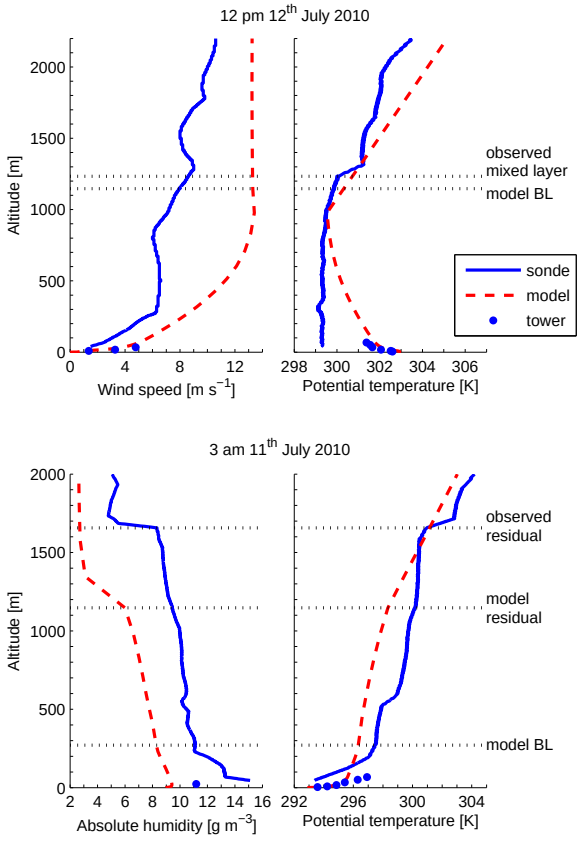

Figure 3. Examples of modelled and observed vertical profiles at 12 p.m. on 12 July (top) and 3 a.m. on 11 July (bottom). Solid lines are data obtained from radiosonde observations, and the dots are 30 min averages from the SMEAR II tower. The model values represent the 30 min during which the soundings were made.

for improving the accuracy of the model close to the top of the boundary layer to be out of the scope of this work. A single radiosonde flight provides a snapshot from a given moment, whilst the model aims to represent average conditions of 30 min for a horizontally homogeneous area. As a consequence the simulated horizontal wind speed profile (Fig. 3a) differs significantly from the observed one. In the model the wind speed increases first rapidly in the surface layer and then more slowly in the boundary layer, having the maximum at the top of the boundary layer, above which it reaches the geostrophic wind speed and stays constant in the free troposphere. The difference in observed and modelled wind speed in the free-troposphere seen in the figure is caused by the difference between the ECMWF reanalysis and the observations and the fact that in the model the wind speed is kept constant above the boundary layer. For accuracy of the reanalysis see Dee et al. (2011).

The lower part of Fig. 3 shows a typical nocturnal stable boundary layer at 3 a.m., which is characterised by a stable layer with strong gradients and a residual layer of the previous day's mixed layer where quantities are almost constant

with altitude. In these types of cases the top of the boundary layer is ambiguous (Zilitinkevich and Mironov, 1996). The model parameterisation sets the ABL depth at a height that coincides with approximately the layer in the observations which is most stable. Above the stable layer an almost neutrally stratified residual layers is clearly visible in the observations. The residual layers shown in the figure are defined as the layer where water vapour concentration is roughly constant with altitude. The model underestimates the residual layer height, which is a consequence of the tendency to underestimate the height of the mixed layer. The different nature of the radiosonde and ground-based observations is evident in the stable layer, and the aim of our model is not to reproduce the profile of the soundings exactly. However, it is obvious that the model underestimates the concentration of water vapour in the air. For the campaign period, the model underestimated the water vapour concentration by 23.7 % on average at 23 m. This underestimation only has a minor effect on the modelled reactivities. A sensitivity test shows that when the water vapour concentration is constrained by the measurements, the reactivity of OH and NO_3 is always smaller than when the modelled water concentration is used. The reactivity of O_3 is also mostly lower, but not always. The maximum changes in the reactivities are 1.4 % for OH, 5 % (but usually 1–2 %) for NO_3 and 0.4 % for O_3.

7.1.2 Surface energy balance

The diurnal averages of the components of the surface energy balance – net radiation, heat flux and storage into the soil, and turbulent fluxes of sensible and latent heat – are presented in Fig. 4. The positive values suggest that the atmosphere is gaining heat from the surface and vice versa for negative values. The net radiation from the model was calculated as the sum of all radiation components (the direct and diffuse global radiation, atmospheric thermal radiation, PAR and NIR reflected and emitted by the vegetative canopy, and the thermal radiation by the soil surface) and is compared to the net radiation measured for 300–40 000 nm. Using the reanalysis values as input for atmospheric thermal radiation (Sect. 5.1) instead of the parameterisation (Sogachev et al., 2002) improved the model performance considerably: RMSE for net radiation improved from 82 to 69 $W m^{-2}$ (for the period studied here). The soil heat flux and storage term in the model would follow exactly what was measured since the values used in the model are based on the observations; hence only observed values are shown.

The observed turbulent fluxes shown in Fig. 4 are obtained with an eddy-covariance system described by Markkanen et al. (2001). Both the average latent and sensible heat flux differ from the observed most of the day, which is mainly due to the limitations of the utilised turbulence closure scheme that performs best under near-neutral stratification. The underestimation of the latent heat flux in the model can also partly be caused by underestimation of water available to evaporate, which further could lead to increased surface temperature and to overestimated sensible heat flux. The low latent heat flux can also play a role in the underestimation of absolute humidity (Fig. 3). In general, the accuracy of the eddy-covariance method varies between 5–20 and 10–30 % for sensible and latent heat flux, respectively (Foken, 2008). Furthermore, the measurements are made in the roughness sublayer, which tends to decrease the observed scalar fluxes (Simpson et al., 1998). Hence, the difference between the model and measured values, especially for the sensible heat flux, is too large to be fully explained by inaccuracy of the eddy-covariance method.

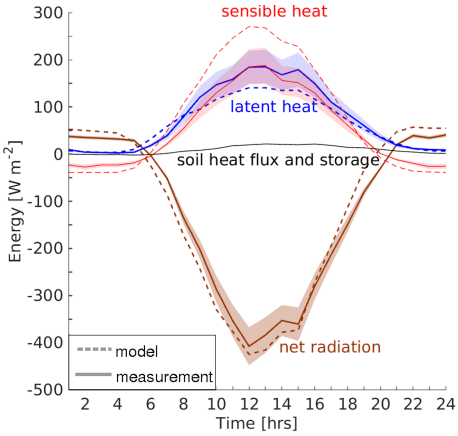

Figure 4. Diurnal averages of the components of the surface energy balance. Net radiation: sum of all radiation components in the model (the direct and diffuse global radiation, atmospheric thermal radiation, PAR and NIR reflected and emitted by the vegetative canopy, and the thermal radiation by the soil surface) compared to the net radiation measured for 300–40 000 nm above the canopy. Heat flux and storage in the soil is the average of four heat plates, and observed values were used as model input. Turbulent fluxes of sensible and latent heat measured with an eddy covariance system at 23.3 m. The shaded areas represent the uncertainty in the measurements, which are estimated to be ±20 % for the heat fluxes and ±10 % for the net radiation.

7.1.3 Turbulent mixing

To validate the turbulence scheme, the observed and simulated friction velocity (u^*) were compared. Friction velocity is defined as the square root of the ratio of momentum flux and air density; thus it describes the amount of turbulent mixing (Stull, 1988, p. 67).

The diurnal mean u^* at each model level for the lowest 40 m, together with an average horizontal wind profile at 1–2 a.m. and p.m., is shown in Fig. 5. The midday profile represents clearly the turbulent conditions, while in the nighttime stratification is typically stable or near neutral (Fig. 5b, c). Inside the canopy the horizontal wind speed and friction velocity decrease rapidly. Above the canopy the wind speed continues to increase until the top of the mixed layer (Fig. 3),

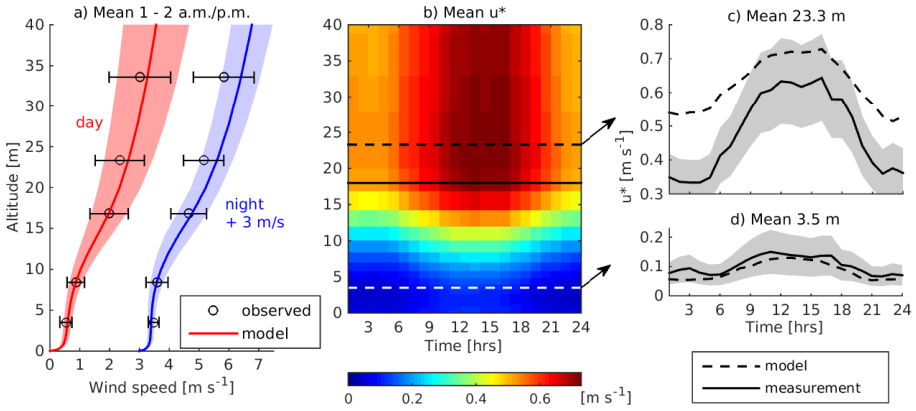

Figure 5. Average wind speed profile ±SD at 1–2 a.m. and p.m. **(a)**. Red and blue lines and area are simulated values for day and night (3 m s^{-1} added for clarity), respectively, black from measurements. Simulated diurnal mean friction velocity (u^*) **(b)**. The top of the canopy is shown with a solid line and the measurement heights of the eddy covariance systems with dashed lines. Observed and simulated mean friction velocity in **(d)** and above the canopy **(c)**. The shaded areas in **(c)** and **(d)** represent the estimated uncertainty of ±20 % **(c)** and ±50 % **(d)**, respectively.

whilst friction velocity has its maximum right above the canopy and slowly decreases towards the top of the boundary layer. The observed values of u^* (Fig. 5c and d) are obtained from eddy-covariance systems at 3.5 and 23.3 m and calculated from the measured covariances of horizontal and vertical wind fluctuations ($\overline{u'w'}$ and $\overline{v'w'}$). At both comparison heights the model reproduces the diurnal behaviour, but the magnitude is overestimated above the canopy, especially at night-time. This is partly due to the strong gradient at the region of the canopy top in the simulations, which causes the comparison to be very sensitive to altitude. Furthermore, the top of the canopy might cause differences just above the canopy (Fig. 5c), since all dynamics caused by scattered tree tops are not necessarily accounted for in a one-dimensional model. Horizontal wind speed increases more rapidly with altitude in the model, which could partly also explain the overestimation of friction velocity by the overestimated wind shear. The turbulence closure scheme is known to perform best under near-neutral stratification. However, the overestimation of friction velocity was found persisting for all stability conditions.

7.2 Comparison of trace gas measurements

In this section we intercompare the measured concentrations of NO, NO_2, O_3 and CO. For the comparison we have also excluded the pollution periods, since the concentrations of these gases are often larger during the pollution events, whereby the uncertainties in the measurements are expected to decrease. For statistical purposes it is therefore better to only consider the same period as our model results.

In general there was satisfactory agreement between the different instruments. The differences between the results (time series in Fig. 6, mean values in Table 1) were within the uncertainty limits in case of the NO and NO_2 data. In

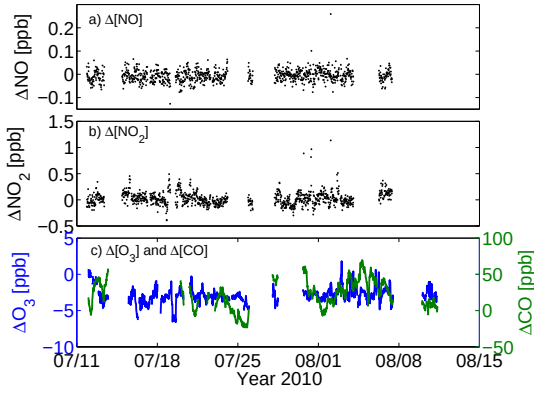

Figure 6. Difference in measured gas concentration of **(a)** NO, **(b)** NO_2 and **(c)** O_3 (blue, left-hand side) and CO (green, right-hand side). The difference is calculated by subtracting the campaign-measured concentrations by the SMEAR II-obtained concentrations.

case of the O_3 concentration results there was a systematic difference of 4 ppb. Also the variabilities in the averaged concentrations were in the same magnitude (Fig. 1). In the CO concentration data there was a distinct variability between the SMEAR II and campaign results. The observed difference (22 ppb) was within the uncertainty limits. There were periodical malfunctions of the SMEAR II instrument causing false readings. During post-processing the SMEAR II data were filtered, but obviously some inconsistency remained in the data.

7.3 Photolysis

We present the measured $J(NO_2)$ and $J(O^1D)$ in Fig. 7 (time series) and in Fig. 8 (scatter plot) together with the

Table 1. Measurement uncertainty and estimates for quality of fit for the measured input gas concentrations. H is height, MES and MEC the estimated total accuracies calculated as a combination of precision and the accuracy of reading for the SMEAR II (MES) and campaign (MEC) instrumentation. DP is the number of measured data points considered, $\overline{S}$ and $\overline{C}$ the SMEAR II-measured (S) and campaign-measured (C) means, SD_S and SD_C the corresponding SD, r Pearson's product-moment correlation coefficient which describes colinearity between measured and modelled parameters, r^2 the coefficient of determination which describes the proportion of the total variance explained by the model, b the slope, a the intercept of linear least-square regression. MSE is the mean square error, $RMSE_s$ systematic RMSE, $RMSE_u$ unsystematic RMSE, RMSE total root mean square error, bias the difference between $\overline{C}$ and $\overline{S}$ and d the index of agreement.

	[NO]	[NO_2]	[O_3]	[CO]
H [m]	24	24	24	24
MES [ppb]	±0.05	±0.09	±1	±25
MEC [ppb]	±0.01	±0.03	±4	±10
DP	1066	1066	1066	833
$\overline{S}$ [ppb]	2.32×10^{-2}	3.64×10^{-1}	3.70×10^{1}	1.20×10^{2}
SD_S [ppb]	3.35×10^{-2}	3.03×10^{-1}	9.89×10^{0}	2.53×10^{1}
$\overline{C}$ [ppb]	2.90×10^{-2}	3.38×10^{-1}	3.99×10^{1}	9.82×10^{1}
SD_C [ppb]	3.28×10^{-2}	2.14×10^{-1}	9.69×10^{0}	1.32×10^{1}
r	6.84×10^{-1}	9.27×10^{-1}	9.94×10^{-1}	6.23×10^{-1}
r^2	4.68×10^{-1}	8.60×10^{-1}	9.89×10^{-1}	3.88×10^{-1}
b	6.98×10^{-1}	1.31×10^{0}	1.02×10^{0}	1.19×10^{0}
a [ppb]	2.89×10^{-3}	-7.94×10^{-2}	-3.51×10^{0}	2.89×10^{0}
MSE [ppb^2]	3.29×10^{-2}	6.72×10^{-1}	8.04×10^{3}	3.48×10^{5}
$RMSE_s$ [ppb]	1.20×10^{-2}	6.24×10^{-2}	2.96×10^{0}	2.23×10^{1}
$RMSE_u$ [ppb]	1.81×10^{-1}	8.17×10^{-1}	8.96×10^{1}	5.89×10^{2}
RMSE [ppb]	1.81×10^{-1}	8.20×10^{-1}	8.97×10^{1}	5.90×10^{2}
Bias [ppb]	-5.89×10^{-3}	2.66×10^{-2}	-2.90×10^{0}	2.16×10^{1}
d	8.18×10^{-1}	9.30×10^{-1}	9.76×10^{-1}	6.21×10^{-1}

Table 2. Measurement uncertainty and estimates for quality of fit for photolysis rates ($J(NO_2)$ and $J(O^1D)$) and the reactivity of OH (R_{OH}). ME is reported measurement uncertainty, $\overline{O}$ and $\overline{P}$ the measured (O) and modelled (P) means, SD_O and SD_P the corresponding SDs and the bias the difference between the mean measured and mean modelled parameter. For the meaning of the remaining symbols, we refer to the description in the Table 1.

	$J(NO_2)$	$J(O^1D)$	R_{OH}	R_{OH}
H [m]	24	24	18	24
ME [%]	∼ 5–8	> 8	16	16
DP	1019	1019	357	320
$\overline{O}$ [s^{-1}]	6.41×10^{-3}*	1.55×10^{-5}*	1.26×10^{1}	1.05×10^{1}
SD_O [s^{-1}]	1.80×10^{-3}*	4.76×10^{-6}*	1.34×10^{1}	9.79×10^{0}
$\overline{P}$ [s^{-1}]	5.37×10^{-3}*	1.55×10^{-5}*	2.59×10^{0}	2.52×10^{0}
SD_P [s^{-1}]	1.88×10^{-3}*	4.99×10^{-6}*	4.96×10^{-1}	4.47×10^{-1}
r	9.00×10^{-1}	9.28×10^{-1}	3.17×10^{-1}	3.49×10^{-1}
r^2	8.10×10^{-1}	8.62×10^{-1}	1.01×10^{-1}	1.22×10^{-1}
b	1.31×10^{0}	1.02×10^{0}	1.17×10^{-2}	1.59×10^{-2}
a [s^{-1}]	-7.94×10^{-2}	-3.51×10^{0}	2.44×10^{0}	2.35×10^{0}
MSE [s^{-2}]	6.72×10^{-1}	8.04×10^{3}	3.59×10^{4}	2.05×10^{4}
$RMSE_s$ [s^{-1}]	6.24×10^{-2}	2.96×10^{0}	1.66×10^{1}	1.25×10^{1}
$RMSE_u$ [s^{-1}]	8.17×10^{-1}	8.96×10^{1}	1.89×10^{2}	1.43×10^{2}
RMSE [s^{-1}]	8.20×10^{-1}	8.97×10^{1}	1.90×10^{2}	1.43×10^{2}
Bias [s^{-1}]	2.66×10^{-2}	-2.90×10^{0}	1.00×10^{1}	8.01×10^{0}
d	9.30×10^{-1}	9.76×10^{-1}	4.33×10^{-1}	4.43×10^{-1}

∗ only noon value

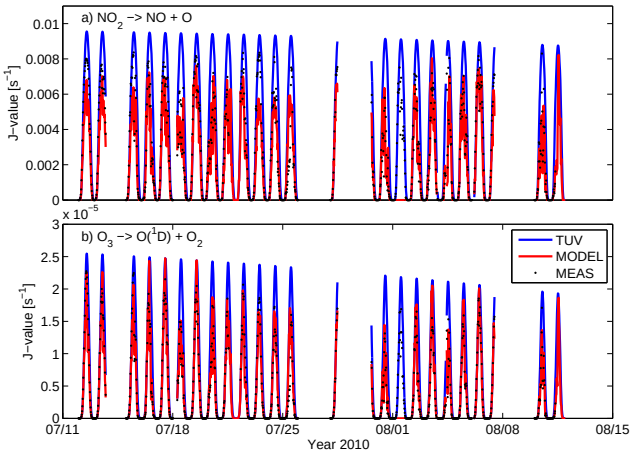

Figure 7. Above-canopy measured (black dots) and SOSAA modelled (red line) photolysis rate for **(a)** $NO_2 \rightarrow NO+O$ and **(b)** $O_3 \rightarrow O(^1D) + O_2$. For comparison, also the TUV (Tropospheric Ultraviolet and Visible Radiation Model) predicted rates are included.

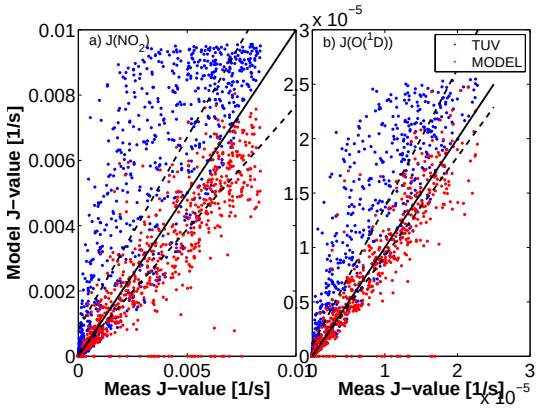

Figure 8. Scatter plots of the measured versus the SOSAA modelled (red dots) and the TUV (Tropospheric Ultraviolet and Visible Radiation Model, blue dots) predicted above-canopy photolysis rates for **(a)** $NO_2 \rightarrow NO + O$ and **(b)** $O_3 \rightarrow O(^1D) + O_2$. The solid lines indicate the 1 : 1 reference line, whereas the broken lines represent the least-squares line.

predicted SOSAA values where we used the parameterisation suggested in Sect. 5.3. For comparison, also the TUV predicted rates, which provide the fastest possible photolysis (since clear sky was assumed), are included. The surface reflectivity was assumed to be independent of wavelength and was fixed to 0.1. The performance of our simple parameterisation is good, even though the conversion factor used is calculated as the median over the entire measurement period. The modelled rates are always found below the TUV clear-sky predicted rates. Different checks for quality of fit are presented in Table 2. On average, the modelled noon photolysis peak of NO_2 is slightly underestimated ($\sim$ 16 %), though when considering the entire day, the difference is larger. Photolysis rates were also obtained near ground, however, not inside the canopy, but instead in a clearing only partly covered by overhanging branches. It is therefore difficult to compare those rates with our predicted below-canopy rates, where we use a canopy penetration factor, which decreases the incoming irradiance when going down through the canopy. At ground the photolysis rates are decreased by $\sim$ 40–80 %. The reduction is by $\sim$ 30–50 % in the measurements.

7.4 Oxidant reactivity

The total reactivities of the three most important atmospheric oxidants (OH, O_3 and NO_3) have been modelled and will be presented here together with the measured OH reactivity. No measurements of O_3 and NO_3 reactivity were conducted during this campaign. Instead we have measurements of the concentrations and production rate of NO_3, which enable a steady-state turnover lifetime to be calculated and compared to the model result. The daily and seasonal oxidation capacity with respect to monoterpenes at SMEAR II has previously been estimated based on measurements and is presented in Peräkylä et al. (2014). The HO_x budget during this campaign has been discussed in detail by Hens et al. (2014). Below we will discuss the daily pattern of the investigated reactivities, together with their vertical profile. In case of the reactivity of OH, we will also discuss the missing OH reactivity and in case of the NO_3 reactivity we will present both the modelled instantaneous reactivity and the calculated steady-state reactivity.

7.4.1 Contribution to the reactivities

We have investigated the compound-specific chemical contributions to the three different oxidant reactivities. The contributions at noon and during night (at 18 m) together with the total reactivities are presented in Table 3. The reactivities toward methane, isoprene and all individual monoterpenes and sesquiterpenes are included separately. Furthermore, according to the MCM chemistry, OH is reacting with 1071 other organic species, while an additional BVOC sink consisting of 437 organic species is included for NO_3, but only 28 other BVOC species react with O_3. The normalised contribution of the individual inorganic compounds to the total inorganic reactivity of the three oxidants that we consider is presented in Fig. 10 as a daily average for the campaign period (at 18 m), while the absolute contributions are visualised in Fig. 11. The inorganic sink of OH is due to reactions with H_2, H_2O_2, O_3, NO, NO_2, SO_2 and CO, while the inorganic sink of O_3 includes three species – OH, NO, and NO_2 – and lastly the inorganic sink of NO_3 includes NO and NO_2.

7.4.2 OH reactivity

The daily averaged profiles of the modelled and measured OH reactivity at 18 and 24 m are presented in Fig. 9b and c.

Table 3. Time-dependent contribution to the investigated instantaneous reactivities. The contribution distributions and total reactivities are given as means for 18 m at noon and at night (2 a.m.) for the OH, O_3 and NO_3 reactivity. The contributions are given with respect to inorganic compounds (see Sect. 7.4 for which compounds are included), methane (CH_4), isoprene (C_5H_8), total and individual monoterpenes ($C_{10}H_{16}$) and sesquiterpenes ($C_{15}H_{24}$) (see Sect. 5.4) together with the resisting organic compounds that the three oxidants are reacting with (see Sect. 7.4 for how many compounds this includes).

	OH reactivity		O_3 reactivity		NO_3 reactivity	
	Noon	Night	Noon	Night	Noon	Night
Total [s^{-1}]	2.79	3.00	1.58×10^{-5}	1.67×10^{-5}	6.07×10^{-2}	6.45×10^{-2}
Inorganics [s^{-1}]	1.18	1.20	1.44×10^{-5}	9.17×10^{-7}	2.68×10^{-2}	1.29×10^{-2}
CH_4 [s^{-1}]	2.71×10^{-1}	2.45×10^{-1}	0	0	0	0
C_5H_8 [s^{-1}]	4.39×10^{-2}	7.18×10^{-3}	5.67×10^{-9}	7.45×10^{-10}	3.07×10^{-4}	4.65×10^{-5}
α-pinene [s^{-1}]	1.02×10^{-1}	1.47×10^{-1}	1.76×10^{-7}	2.32×10^{-7}	1.22×10^{-2}	1.75×10^{-2}
β-pinene [s^{-1}]	3.56×10^{-2}	7.87×10^{-2}	6.86×10^{-9}	1.47×10^{-8}	1.10×10^{-3}	2.40×10^{-3}
Δ^3-carene [s^{-1}]	1.44×10^{-1}	2.59×10^{-1}	6.29×10^{-8}	1.08×10^{-7}	1.53×10^{-2}	2.63×10^{-2}
Limonene [s^{-1}]	1.00×10^{-2}	1.38×10^{-2}	1.30×10^{-8}	1.63×10^{-8}	7.44×10^{-4}	9.89×10^{-4}
Cineol [s^{-1}]	3.40×10^{-4}	4.34×10^{-4}	4.68×10^{-12}	5.93×10^{-12}	5.24×10^{-9}	6.67×10^{-9}
Other $C_{10}H_{16}$ [s^{-1}]	1.25×10^{-2}	1.82×10^{-2}	2.06×10^{-8}	2.73×10^{-8}	1.50×10^{-3}	2.20×10^{-3}
Total $C_{10}H_{16}$ [s^{-1}]	3.05×10^{-1}	5.16×10^{-1}	2.79×10^{-7}	3.98×10^{-7}	3.08×10^{-2}	4.94×10^{-2}
β-caryophyllene [s^{-1}]	1.50×10^{-2}	4.20×10^{-3}	8.76×10^{-7}	2.46×10^{-7}	1.40×10^{-3}	4.04×10^{-4}
Farnesene [s^{-1}]	3.40×10^{-3}	9.59×10^{-4}	1.96×10^{-7}	5.50×10^{-8}	3.22×10^{-4}	9.02×10^{-5}
Other $C_{15}H_{24}$ [s^{-1}]	1.00×10^{-3}	2.90×10^{-4}	5.85×10^{-8}	1.67×10^{-8}	9.63×10^{-5}	2.73×10^{-5}
Total $C_{15}H_{24}$ [s^{-1}]	1.94×10^{-2}	5.42×10^{-3}	1.13×10^{-6}	3.18×10^{-7}	1.86×10^{-3}	5.21×10^{-4}
Other VOCs [s^{-1}]	1.25	1.26	2.86×10^{-8}	3.14×10^{-8}	9.33×10^{-4}	1.65×10^{-3}

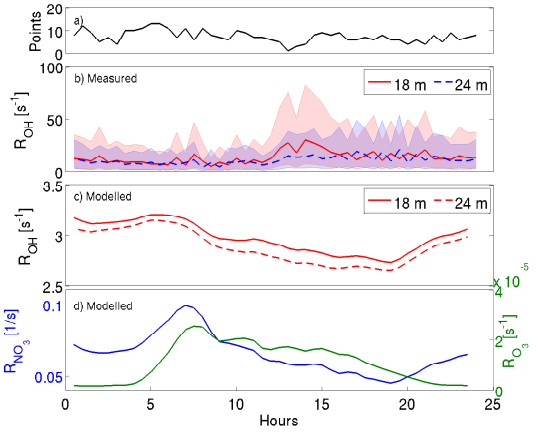

Figure 9. Daily averaged measured and modelled total OH reactivity together with daily averaged modelled total O_3 and NO_3 reactivity. **(a)** indicates the number of measured half hour data points that has been used for the averaging of the measured reactivity, **(b)** measured OH reactivity at 18 (solid red line) and 24 m (dashed blue line), where the shaded areas are the 75 and 25 percentiles, **(c)** modelled OH reactivity at 18 m (solid red line) and at 24 m (dashed red line) and **(d)** modelled reactivities of NO_3 (blue line, left-hand side on y axis) and O_3 (green line, right-hand side on y axis).

The modelled reactivities include all values modelled when the pollution periods have been filtered out, while the measured reactivities contains fewer data due to instrumental disruption. It is clear that the modelled reactivity is much lower than the measured (see also below). During noon–early afternoon, the difference in measured above- and in-canopy reactivity increases and the in-canopy reactivity is found to be almost twice that of the above-canopy reactivity. The modelled in-canopy reactivity is consistently higher than the above-canopy reactivity. While the modelled OH reactivity shows little variability throughout the day (minimum / maximum reactivity = 0.85), excluding a small late afternoon dip due to lower ambient monoterpene concentrations (Mogensen et al., 2011), the measured reactivity shows a stronger daily trend (minimum / maximum reactivity = 0.17) with a noon–early afternoon maximum. However, as indicated in Fig. 9a, very few measured data points were used for the averaging of the reactivity in the time slot where the peak is observed. The OH reactivity has previously been both measured and modelled at SMEAR II, and also then a small early afternoon maximum was seen from the observations, while the modelled reactivity was found to be more or less constant (Mogensen et al., 2011; Sinha et al., 2010). These new simulations, however, show larger daily variability than in the study by Mogensen et al. (2011), which is mostly due to improvements in the meteorological scheme. A combination of the different schemes for meteorology, emission and chemistry was validated by Mogensen et al. (2011). This study showed good agreement between measured and modelled monoterpene concentrations for several heights.

The apportioned and total instantaneous reactivity of OH are reported in Table 3. For the list of specific inorganic

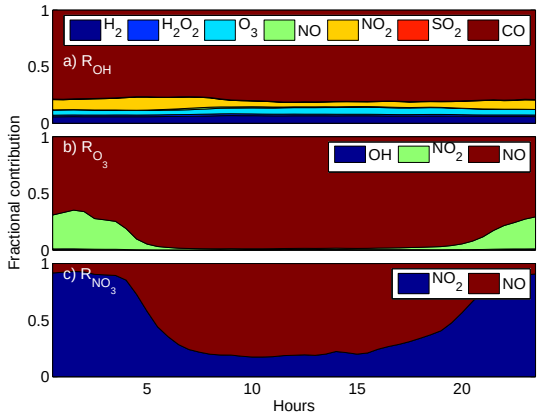

Figure 10. The daily averaged fractional contribution of individual inorganic compounds to the total inorganic reactivity of OH **(a)**, O_3 **(b)** and NO_3 **(c)** at 18 m.

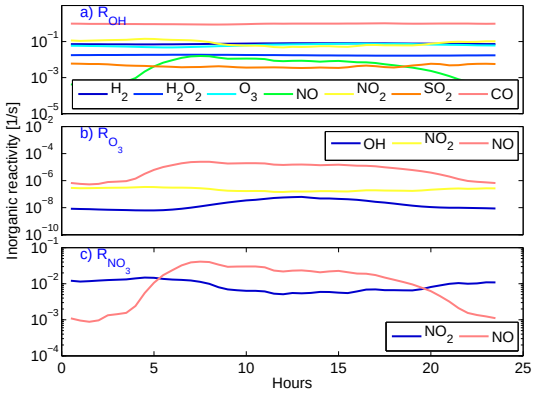

Figure 11. The daily averaged reactivity of OH **(a)**, O_3 **(b)** and NO_3 **(c)** at 18 m due to reactions with specific individual inorganic compounds. Please note the log scale on the *y* axis.

compounds, and total number of compounds that OH reacts with, we refer to Sect. 7.4.1. The contribution from inorganic compounds and methane is more or less constant at both shown times, and together they make up about half of the total OH reactivity. The contribution from the individual inorganic compounds to the total inorganic reactivity is shown in Fig. 10a, while their absolute reactivities are presented in Fig. 11a. We observe that the contributions from the specified inorganic compounds do not vary significantly throughout the day. One exception is the contribution from the reaction with NO_2, which is greatest during night-time. By far the largest contribution is made up by the reaction with CO ($\sim 80\,\%$). The contributions from H_2, O_3 and NO_2 are similar ($\sim 5\,\%$). The contribution from isoprene is 5 times larger during day than night, since the emission of isoprene is controlled by light. However, the reactivity towards isoprene is at all times insignificant due to the very low ambient concentration at the SMEAR II station (campaign average was 1.8×10^8 molecules cm^{-3}). The reactivity attributable to sesquiterpenes is even lower, which is also due to low emissions but also due to competing reactivity towards other compounds (e.g. O_3). Since SMEAR II is a monoterpene-dominated environment, the reactivity of OH due to reactions with these terpenes is significant and they make up the largest fraction of the OH reactivity due to primary emitted terpenoids (on average 89 % at 18 m). Since monoterpene emissions are driven by temperature and the night-time temperatures were high during the campaign, while the turbulent mixing was slow, the OH reactivity due to monoterpenes is clearly largest during night-time. Rinne et al. (2012) studied the effect of oxidation chemistry on above-canopy biogenic fluxes during the HUMPPA campaign and found that the chemical degradation had a major effect on the fluxes of sesquiterpenes, while the monoterpene fluxes were only affected during night-time. We found that the largest contribution was due to oxidation products (called "other VOCs" in Table 3), which were responsible for slightly more than two-fifths of the total reactivity. By far most of these compounds are not usually measured and they are generally not included in the calculated OH reactivity (e.g. Nölscher et al., 2012a).

The vertical profile of the OH reactivity covering from the ground to approximately 10 m above the canopy is presented in Fig. 12a as a daily average for the campaign period. The vertical profile of the OH reactivity is somewhat different than the findings for summer 2008 (Mogensen et al., 2011), which is partly due to an improvement of the meteorological scheme with more vertical mixing as well as due to updates in the emission and chemistry schemes. As in Mogensen et al. (2011) we find that the highest OH reactivity is during night, which is due to the shallow boundary layer. When the sun rises, the residual layer breaks up, and the OH reactive compounds are diluted in a larger volume. Also, a continuously high reactivity is found in the entire canopy. After the break-up of the ABL, the OH reactivity is still high(er) in the crown of the canopy, near the emitting source. The difference between night-time and daytime OH reactivity is approximately $0.5\,s^{-1}$, which is 15 % of the night-time OH reactivity.

A detailed analysis of the measured, calculated (by using measured gas concentrations of OH reactive compounds) together with the missing (the difference between measured and calculated or modelled OH reactivity) OH reactivity for the HUMPPA-COPEC-10 campaign is provided by Nölscher et al. (2012a). These researchers divide the measured period into "stressed", "transported pollution" and "normal boreal conditions" (which is not the same as our period, but instead covers 30 July–10 August) and report a missing OH reactivity of 58 % for the last mentioned category, whereas for "stressed" boreal conditions a missing OH reactivity of 89 % was determined. Nölscher et al. (2012a) also give suggestions for potential missing sources. We calculate the missing OH reactivity at 18 m as $10.0\,s^{-1} = 64.7\,\%$ (mean) and $4.7\,s^{-1} = 70.0\,\%$ (median), and at 24 m as $8.0\,s^{-1} = 68.7\,\%$

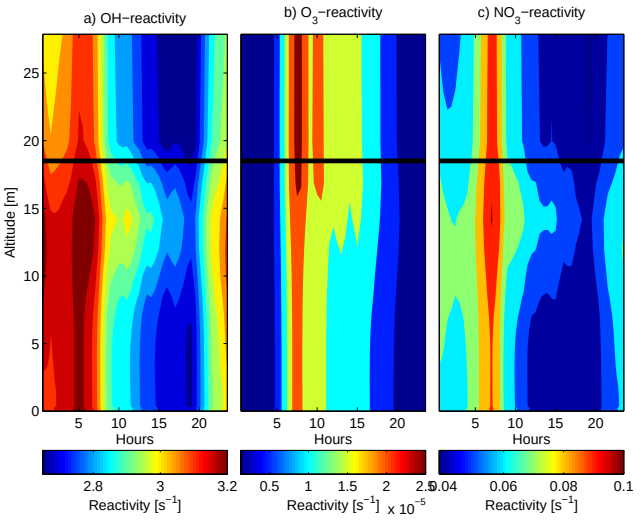

Figure 12. Daily averaged vertical total reactivity of OH **(a)**, O_3 **(b)** and NO_3 **(c)**. The top of the canopy is indicated by a black solid line.

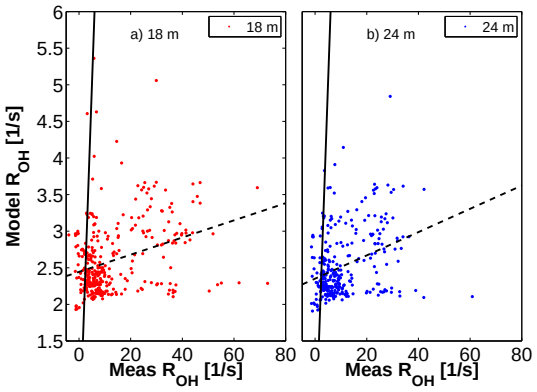

Figure 13. Scatter plots of the measured versus the modelled reactivity of OH at 18 **(a)** and 24 m **(b)**. The solid lines indicate the 1 : 1 reference line, whereas the broken lines represent the least-squares line.

(mean) and $4.4\,s^{-1} = 67.7\,\%$ (median). As the simulated OH reactivity shows less variance throughout the day, the variability in the missing OH reactivity with time (not shown) is mostly due to the measured OH reactivity. As already pointed out by Mogensen et al. (2011), even though the meteorological description is satisfactory, the modelled forest is too homogeneous to capture the variability in the measured OH reactivity. While the modelled OH reactivity is only slightly higher than the predicted for the BFORM campaign (Mogensen et al., 2011), the missing OH reactivity is found to be larger during the HUMPPA-COPEC-10 campaign, which is most probably due to higher temperatures and therefore a higher concentration of unknown BVOCs. Nölscher et al. (2012a) also calculated the OH reactivity due to some measured anthropogenic gases (xylene, ethylbenzene, acetonitrile, toluene, butane, pentane, PAA and PAN) that are not included in our model simulations, due to lack of emission estimates. The missing reactivity of $4.7\,s^{-1}$ (median missing fraction for 18 m) corresponds to a concentration on the order of approximately 9×10^{10} molecules cm^{-3} for a missing compound that has a similar reaction rate with OH as α-pinene. Nölscher et al. (2012a) found that these anthropogenic compounds are not significant contributors to the OH reactivity during non-polluted times as we have considered here. The exclusion of these anthropogenic gases can therefore not explain our missing OH reactivity. Further uncertainty estimations are provided in Table 2, and correlation plots are shown for both heights in Fig. 13. All parameter values in the table are calculated based on only those time periods when measurement data were available (after excluding the pollution periods). We observe that the bias is largest at 18 m, inside the canopy, therefore closer to the emission source. Furthermore, almost the entire RMSE is unsystematic, indicating that it is not a single parameter that drives the missing sink term. One should be aware that evaluating modelled OH reactivity with observed is not a good measure for quantifying the quality of a model, since it is well known that the missing OH reactivity is large, and often larger than the known fraction, especially in forested areas (e.g. Stone et al., 2012, and references therein). Many investigators have speculated on the origin of the missing reactivity, and it is mostly thought that the difference between measured and modelled or calculated OH reactivity is due to unknown organic compounds (e.g. Sinha et al., 2010; Nölscher et al., 2012a; Stone et al., 2012). Since the SMEAR II site is well studied with respect to tree emissions (e.g. Hakola et al., 2003; Hakola et al., 2006; Tarvainen et al., 2005; Bäck et al., 2012; Aalto et al., 2014), we are quite confident which specific VOCs are emitted, and it seems unlikely that our missing OH reactivity is due to emitted VOCs (which are measurable with gas chromatograph – mass spectrometer (GC-MS) and proton transfer reaction – mass spectrometer (PTR-MS)). The missing reactivity is more likely due to either emitted VOCs that are not detectable by GC-MS and PTR-MS and/or unknown oxidation products of the known emitted compounds.

7.4.3 NO_3 reactivity

The daily averaged profile of the reactivity of NO_3 at 18 m is presented in Fig. 9d (left y axis). The NO_3 reactivity is approximately 1 order of magnitude less than the modelled OH reactivity. The NO_3 reactivity steadily increases from around 7 p.m. (reactivity of $\sim 0.05\,s^{-1}$) until midnight where it stays approximately constant ($\sim 0.07\,s^{-1}$) until 5 a.m. where it increases again and peaks around 7 a.m. ($\sim 0.1\,s^{-1}$). Within the following 2 h the NO_3 reactivity decreases rapidly (with $\sim 0.03\,s^{-1}$) followed by a more steady decrease until 7 p.m. The averaged maximum variation throughout the day in the NO_3 reactivity is approximately 50 %, with higher reactivities during night (see below when the contribution to the individual reactivities is discussed).

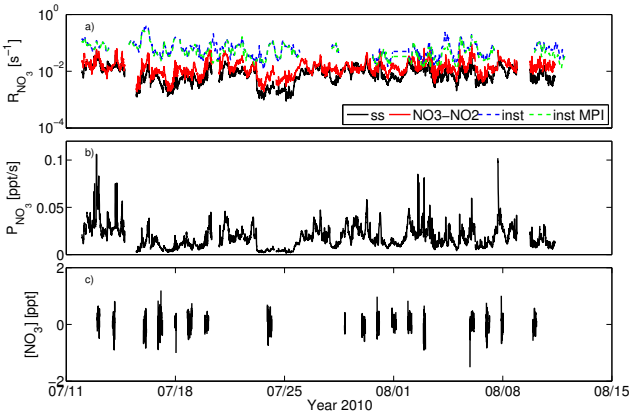

Figure 14. (a) The steady state (ss, in black) and instantaneous (inst, in dashed blue, when using SMEAR II NO_x concentrations, inst MPI, in dashed green, when using MPI NO_x concentrations) NO_3 reactivity (R_{NO_3}) together with the corrected steady-state reactivity where also the reactions of NO_3 with NO_2 have been taken into account (NO_3–NO_2, in red), **(b)** the production term ($P_{NO_3} = k_6[NO_2][O_3]$) of NO_3 and **(c)** the measured concentration of NO_3 ($[NO_3]$). Please note the log scale in the **(a)** section.

The contributions to the reactivity together with the total reactivity of NO_3 are presented in Table 3. For the list of specific inorganic compounds, and total number of compounds that NO_3 reacts with, we refer to Sect. 7.4.1. The inorganic contribution to the NO_3 reactivity is largest during daytime (44 % vs. 20 % during night-time). The contribution from the individual inorganic compounds to the total inorganic NO_3 reactivity is shown in Fig. 10c, while their absolute reactivities are shown in Fig. 11c. During night-time the inorganic instantaneous reactivity is due to reaction with NO_2, while the daytime inorganic reactivity is due to reactions with NO. The other main contributors to the total NO_3 reactivity are the emitted monoterpenes. During daytime, their contribution is about 50 %, though during night the contribution from the monoterpenes is 77 %. The difference in daytime vs. night-time monoterpene concentration is partly due to difference in emission (due to difference in temperature and exposed light) and partly due to turbulent mixing. The dominant monoterpenes are at all times α-pinene and Δ^3-carene. The inorganic contribution, together with the contribution from directly emitted monoterpenes, accounts for 96 % of the total instantaneous reactivity. Known oxidised BVOCs are therefore insignificant in our simulations of the NO_3 reactivity. Organic atmospheric chemistry involving reactions with the NO_3 radical has been much less studied than the chemistry of OH, but recent studies suggests its importance (e.g. Browne and Cohen, 2012; Browne et al., 2014). Due to this unexplored chemistry, it is therefore expected that the NO_3 reactivity due to reactions with oxidised VOCs is significantly larger than simulated here.

The vertical profile of the NO_3 reactivity covering from the ground to approximately 10 m above the canopy is presented in Fig. 12c as a daily average for the campaign period. The pattern of the vertical NO_3 reactivity is somewhat similar to the vertical OH reactivity, since the main sink of NO_3 is the monoterpenes that are also emitted during the warm nights. As also seen in the vertical profile for the OH reactivity, the NO_3 reactivity peaks in the canopy crown, close to the emission source. Since the only significant organic source is the primary emitted monoterpenes, the difference between daytime and night-time reactivity is larger for NO_3 than OH.

The concentration of NO_3 was measured (Fig. 14c) on 18 nights during the HUMPPA-COPEC-10 campaign. The low NO_x levels and large biogenic emissions (mainly monoterpenes) resulted in NO_3 mixing ratios which were below the instrumental detection limit (< 1 ppt in 10 min averaging). On average, the model predicted NO_3 night-time concentrations of 0.8 ppt. In order to calculate the steady-state reactivity (R_{ss}) of NO_3 during the HUMPPA campaign, we have taken an upper limit of 0.5 ppt NO_3 for the whole campaign and divided it by the production term ($P_{NO_3} = k_6[NO_2][O_3]$, Fig. 14b), resulting in a lower limit to the R_{ss}. The results are shown in Fig. 14a. In order to make this result comparable to the instantaneous reactivity, which the model generates, we have also added a term that accounts for the reactions of NO_3 with NO_2 (red line in Fig. 14a). The red line is thus $R_{ss} + k_{NO_2+NO_3}[NO_2]$. We call this the corrected steady-state reactivity, R_{ss} (cor). The variability in the calculated steady-state reactivity of NO_3 is due to the production term (Fig. 14b). In Fig. 14a we show both the instantaneous reactivity of NO_3 modelled using the SMEAR II-obtained NO_x concentrations (inst) and the NO_x concentrations measured by MPI (inst MPI, which is our default). In general, the model over-predicted the measured (and corrected) NO_3 reactivity (on average by a factor 4–5), but on some occasions reasonable agreement was obtained (e.g. on 3 August). On average, the instantaneous NO_3 reactivity was 0.069 s^{-1} (lifetime of 14 s) when using SMEAR II NO_x concentrations and 0.058 s^{-1} (lifetime of 17 s) when using MPI NO_x concentrations, while the steady-state reactivity was 0.0089 s^{-1} (lifetime of 113 s), and the corrected steady-state reactivity was found to be 0.015 s^{-1} (lifetime of 68 s). There are several possible explanations for the difference between the modelled reactivity (R_{inst}) and that based on measurements of NO_3 concentrations (R_{ss} (cor)). Though the averaged modelled night-time NO_3 concentration was 0.8 ppt, the concentration was simulated to be significantly lower than the 0.5 ppt taken as the upper limit for the calculations of R_{ss} (cor) on several nights. Alternatively, the steady-state analysis is only valid when production and loss terms are balanced. For NO_3, achieving steady state can take several hours after sunset, depending on the size of its sink reactions. In this campaign, where the NO_3 sinks are clearly quite large, this should, however, not be an issue. A further explanation is that the trace gases that act as sinks for NO_3 are overestimated in the model. These sinks are largely terpenes and their concentrations, which are based on an emission model,

can contribute to the discrepancy – though in which direction the model bias might go is unclear. Further, we can consider the effects of recycling NO_3 or the effects of unknown NO_3 sources. So far we have considered only the reaction of NO_2 with O_3 as source of NO_3 in the calculation of its steady-state lifetime. Any other reaction that forms NO_3 would result in an underestimation of the NO_3 reactivity for a given steady-state concentration. Similarly, if there are routes to NO_3 reformation from the organic nitrates formed in the initial reactions with terpenes, this will have the effect of enhancing the modelled, instantaneous reactivity compared to that obtained from a steady-state analysis. Further measurements of NO_3 steady-state concentrations (above the detection limit) and reactivity and comparison with modelled instantaneous reactivity in the boreal forest would be useful in order to resolve this issue. Direct measurement of the NO_3 lifetime in this environment would be most informative and is the subject of ongoing instrument development with a summer campaign at this site planned for the near future.

7.4.4 O_3 reactivity

The daily averaged profile of the reactivity of O_3 at 18 m is presented in Fig. 9d (right y axis). The O_3 reactivity shows an early morning peak (sharp build-up from 5 a.m. until $\sim$ 8 a.m.) and the reactivity is generally higher during daytime. This is due to the fact that the known O_3 sink mainly consists of inorganic compounds (see below) and their concentration is largest at the beginning of the day. The largest difference in the O_3 reactivity throughout the day is found between $\sim$ 8 a.m. ($\sim 2.5\times10^{-5}\,s^{-1}$) and 8 p.m. ($\sim 2\times10^{-6}\,s^{-1}$), and the reactivity is close to constant from 8 p.m. to 5 a.m. The O_3 reactivity is approximately 5 orders of magnitude less than the modelled OH reactivity, which of course informs us that O_3 is much less reactive than OH; however, we also need to take the concentration of our respective oxidants into consideration when evaluating their relative importance (Sect. 7.4.5).

The contributions to the O_3 reactivity together with the total reactivity of O_3 are presented in Table 3. For the list of specific inorganic compounds, and total number of compounds that O_3 reacts with, we refer to Sect. 7.4. Independent of time, the controlling O_3 sink is by far the inorganic compounds ($>$ 90 % of the total sink). The remaining O_3 reactivity is made up by reactions with monoterpenes ($<$ 2 % at noon, $\sim$ 2 % during night) and sesquiterpenes ($\sim$ 7 % at noon and $<$ 2 % at night). As in the case of the NO_3 reactivity, known oxidised BVOCs are also insignificant for our simulations of the O_3 reactivity. However, the chemistry of O_3 has also received much less attention than the chemistry of OH, and we therefore expect that O_3 undergoes many important reactions in the atmosphere (e.g. Ehn et al., 2014), which are still to be discovered. We therefore expect that the O_3 reactivity due to reactions with oxidised VOCs is significantly larger than simulated here. The contribution from the individual inorganic compounds to the total inorganic O_3 reactivity is shown in Fig. 10b, and their absolute reactivities are presented in Fig. 11b. At all times, the main fraction of the inorganic O_3 reactivity is due to reaction with NO. During daytime, NO accounts for $\sim$ 98 % of the total inorganic O_3 reactivity. During night-time NO_2, however, also plays a role, since its contribution to the total inorganic reactivity is $\sim$ 30 %. The inorganic O_3 reactivity due to reaction with OH is at all times small ($>$ 0.5 %).

The vertical profile of the reactivity of O_3 covering from the ground to approximately 10 m above the canopy is presented in Fig. 12b as a daily average for the campaign period. The vertical profile of the O_3 reactivity is opposite of that of the two other oxidant reactivities, due to the main sink of O_3, which consists of inorganic compounds. As shown in Fig. 10b O_3 reacts with NO_x and these are mostly transported to the site.

Since the OH reactivity is highly underestimated due to missing sinks, it is also possible that our modelled O_3 and NO_3 reactivities are underestimated due to potentially missing sinks (Wolfe et al., 2011, and references therein).

7.4.5 Relative oxidative strength

O_3 and NO_3 reactivities have not received nearly as much attention as the OH reactivity. To our knowledge, direct total NO_3 reactivity has never been measured, but the steady-state NO_3 reactivity has been calculated, but mostly in environments very different to SMEAR II (Brown et al., 2011, and references therein). Crowley et al. (2010b) measured at a mountain site surrounded by spruce forest and reported steady-state NO_3 reactivities that were about an order of magnitude lower than ours. Ozone has been, and still is, a hot topic, due to its unresolved canopy flux. The non-stomatal ozone flux usually makes up more than half of the total ozone flux, but it seems that gas-phase chemical reactions can only account for a few percentages of the flux (e.g. Rannik et al., 2012; Wolfe et al., 2011). Until now there has been only one publication about direct measurements of O_3 reactivity, in which the author measured the reactivity in the lab (Matsumoto, 2014). Unfortunately, the detection limit of that instrument is so high that ambient measurements are impossible. Park et al. (2013) have developed a new method called ORMS (Ozone Reactivity Measurement System) and tested this in ambient conditions during the SOAS (Southeast Oxidant and Aerosol Study) campaign in summer 2013.

When considering the importance and strength of an oxidant, one should not only focus on its reactivity but also consider its concentration. We evaluate the oxidation strength (OS, or rate of removal) of the oxidant (OX) by multiplying its concentration ([OX]) by its reactivity towards organic compounds ($R_{OX,org}$):

$$OS_{OX} = R_{OX,org} \times [OX]. \quad \text{(R13)}$$

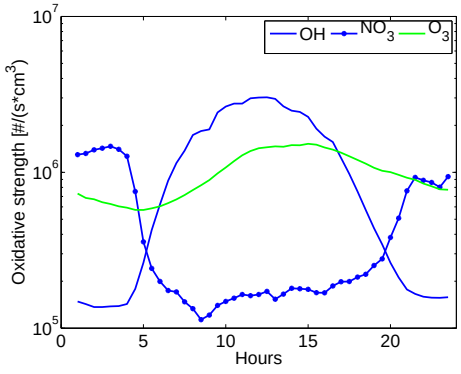

Figure 15. The daily averaged oxidation strength (see Sect. 7.4.5 for definition) of OH (blue line), O_3 (green line) and NO_3 (blue dotted line) at 18 m. Please note the log scale on the *y* axis.

The time-dependent oxidant strength of each of the oxidants considered is illustrated in Fig. 15, and the 24 h integrated oxidation strength is $9.90 \times 10^{+10}$ molecule cm^{-3} for OH, $4.35 \times 10^{+10}$ molecule cm^{-3} for NO_3 and $8.55 \times 10^{+10}$ molecule cm^{-3} for O_3. During daytime, OH is capable of removing compounds much more than the two other oxidants. From around midnight till about 4:30 a.m. NO_3 is the dominant remover of organic compounds, whereas O_3 slightly prevails for less than an hour around 5 a.m. and for a few hours in the early evening. O_3 is by itself not the fastest oxidant at any time; however, at times, O_3 removes reactants more than other oxidants, since it is much more abundant in concentration at the site. The daily patterns of the oxidant strength of all oxidants are mainly controlled by the daily pattern of the oxidant concentration. The campaign-averaged O_3 concentration is depicted in Fig. 1, and we expect that the major night-time removal process of O_3 is by deposition (Rannik et al., 2012).

When evaluating this relative oxidative strength or rate of removal, we should keep a few things in mind. Firstly, we know that we are underestimating the OH reactivity with ~ 65 %, while it is uncertain how large a fraction of the NO_3 and O_3 reactivity we are underestimating. As mentioned previously, the chemistry involving NO_3 and O_3 has been much less studied than the OH chemistry; thus the missing reactivities of NO_3 and O_3 have the potential to be large. Secondly, we have to evaluate the concentration of the oxidants. The concentration of O_3 is taken from measurements. As seen from the intercomparison in Sect. 7.2, the difference was ~ 10 %. This propagates linearly into the uncertainty in the oxidative strength. The concentration of NO_3 is mostly determined by NO_2 (source of NO_3), which is from measurements, O_3 (source of NO_3), which is also from measurements, and finally the monoterpenes (sink of NO_3), which are predicted. It is difficult to evaluate the correctness of the predicted NO_3 concentration, since the measured concentration was mostly below detection limit. Lastly, we have only considered the *strength* of the respective oxidants, which basically means at what rate the oxidant is capable of removing organic compounds from the atmosphere, but we also have to consider the variety of compounds that the oxidants are reacting with. In our chemistry scheme, which includes known chemical reactions, OH reacts with 1082 organic compounds, whereas NO_3 reacts with 448 and O_3 only with 38 species of organic origin. When considering known chemistry, OH therefore has the capacity to clean the atmosphere of much more compounds than the other oxidants. Further, we have to consider what kind of organic compounds it is that our oxidants are reacting with. O_3 almost only participates in the first oxidation step of primary emitted organic compounds (especially sesquiterpenes), though O_3 also reacts with some second or higher generation products from primary emitted compounds (e.g. methacrolein and methyl vinyl ketone). Ehn et al. (2014) recently showed that O_3 participates in the production of ELVOCs (extremely low volatility compounds) which, due to their extremely low volatility, condense immediately unto aerosol particles, which are later lost from the atmosphere via deposition. O_3 is thereby capable of removing carbon from the atmosphere. The primary role of NO_3 is to oxidise directly emitted monoterpenes (first oxidation step). The main path for NO_3 to remove carbon from the atmosphere is by oxidation of terpenes to soluble nitrates which can be washed out. OH has the capacity to remove carbon, since it has the capability of oxidising compounds until the compounds have such a low vapour pressure that they go into the particle phase and then later can deposit out of the atmosphere. As a final remark, we therefore emphasise that the oxidative strength is not equal to the oxidative importance.

8 Conclusions

Using a 1-D chemistry transport model we have performed the following:

– Validation of the full vertical profile with sonde observations showed a tendency to underestimate the depth of the mixed layer and, consequently, also the depth of the night-time residual layer. The absolute humidity in the model was lower than measured. The largest discrepancies of surface energy balance were with the sensible and latent heat fluxes, reflecting the challenge of modelling turbulent fluxes. Evaluating the momentum flux showed satisfactory agreement, and we can conclude that the meteorology module works well.

– We discussed the model uncertainty due to use of measured inorganic gases by intercomparison of the gas concentrations obtained by different measurement techniques. Mostly the gas concentrations were within measurement uncertainty. The largest problem seems to

arise due to the high detection limit and low concentration of NO_x.

– We aimed and managed to successfully create a simple conversion for measured spectral irradiance to actinic flux only based on measurements of photolysis frequency of NO_2 and O_3 (to form O^1D). We showed that the modelled rates compared well with the measured (with index of agreement of 0.93 and 0.98).

– For the first time we have modelled the reactivity of O_3 and NO_3 and compared those to the reactivity of OH. We conclude that OH is the main cleaning agent of organic compounds in the atmosphere. We find that OH is approximately 1 order of magnitude more reactive than NO_3 and 5 orders of magnitude more reactive than O_3 when considering the total reactivity.

  We introduced a term that we call *oxidative strength* that takes both the reactivity towards organic compounds and the concentration of an oxidant into account. It describes the rate at which a given oxidant is capable of removing organic compounds from the atmosphere. We show that OH is the strongest oxidant at our boreal site during daytime, while NO_3 is strongest during nighttime. O_3 competes with OH and NO_3 during short periods in the early morning and evening.

  We observed little difference between modelled in-canopy and above-canopy reactivity. The largest difference in reactivity when considering the full day and canopy was $\sim 15\,\%$ in case of OH, $\sim 50\,\%$ for NO_3 and about a factor of 3 in case of O_3.

  In the model, about 50 % of the OH reactivity was due to inorganic compounds and methane, $\sim 14\,\%$ due to reactions with primary emitted monoterpenes, while about 44 % was due to oxidised biogenic volatile organic compounds. When comparing the modelled OH reactivity to the measured, we find a large discrepancy ($\sim 65\,\%$) which is very common in this type of environment. Most probably the actual main sink of OH is therefore not the modelled inorganic compounds, but instead unaccounted hydrocarbons. Almost the entire reactivity of O_3 was due to inorganic compounds. In case of NO_3, $\sim 37\,\%$ of the reactivity was accounted for by inorganic compounds, while the remaining reactivity was mostly due to first-order reactions with monoterpenes. NO_2, which was included in the inorganic sink term, is, however, an instantaneous sink of NO_3 and it does therefore not control the boreal NO_3 concentrations.

– Furthermore, we performed the first steady-state lifetime calculations of NO_3 in a boreal forest. We obtained a summertime steady-state reactivity of NO_3 on the order of $\sim 0.009\,s^{-1}$ (campaign average), which corresponds to a steady-state lifetime of 113 or 68 s if loss due to reaction with NO_2 is considered. For comparison, the averaged instantaneous NO_3 lifetime was calculated to be 14–17 s.

Acknowledgements. The authors are very grateful for the HUMPPA-COPEC-10 team from Helsinki University and MPI Mainz for providing data for which this study would not be possible. We would like to thank the following researchers personally: Christian Breitenberger, Birger Bohn, Horst Fischer, Rainer Königstedt, Raoul Axinte, Uwe Parchatka and Zeinab Hosaynali-Beygi. D. Mogensen would like to personally thank Li Liao and Putian Zhou for technical help. Furthermore, we thank the Finnish Center of Excellence (FCoE), the Helsinki University Centre for Environment (HENVI) and the Cryosphere–Atmosphere Interactions in a Changing Arctic Climate (CRAICC) for financial support and the CSC – IT Center for Science Ltd for computational resources. Finally D. Mogensen would like to thank the Doctoral Program in Atmospheric Sciences (ATM–DP) for funding of doctoral studies and also the Danish Chemical Society for other financial support.

Edited by: S. M. Noe

References

Aalto, J., Kolari, P., Hari, P., Kerminen, V.-M., Schiestl-Aalto, P., Aaltonen, H., Levula, J., Siivola, E., Kulmala, M., and Bäck, J.: New foliage growth is a significant, unaccounted source for volatiles in boreal evergreen forests, Biogeosciences, 11, 1331–1344, doi:10.5194/bg-11-1331-2014, 2014.

Anthes, R. A.: Data assimilation and initialization of hurricane prediction models, J. Atmos. Sci., 31, 702–719, 1974.

Atkinson, R.: Gas-phase tropospheric chemistry of organic compounds, J. Phys. Chem. Ref. Data, 2, 1–216, 1994.

Atkinson, R., Baulch, D. L., Cox, R. A., Crowley, J. N., Hampson, R. F., Hynes, R. G., Jenkin, M. E., Rossi, M. J., and Troe, J.: Evaluated kinetic and photochemical data for atmospheric chemistry: Volume I – gas phase reactions of O_x, HO_x, NO_x and SO_x species, Atmos. Chem. Phys., 4, 1461–1738, doi:10.5194/acp-4-1461-2004, 2004.

Bäck, J., Aalto, J., Henriksson, M., Hakola, H., He, Q., and Boy, M.: Chemodiversity of a Scots pine stand and implications for terpene air concentrations, Biogeosciences, 9, 689–702, doi:10.5194/bg-9-689-2012, 2012.

Bertram, T. H., Thornton, J. A., Riedel, T. P., Middlebrook, A. M., Bahreini, R., Bates, T. S., Quinn, P. K., and Coffman, D. J.: Direct observations of N_2O_5 reactivity on ambient aerosol particles, Geophys. Res. Lett., 36, L19803, doi:10.1029/2009GL040248, 2009.

Bohn, B., Corlett, G. K., Gillmann, M., Sanghavi, S., Stange, G., Tensing, E., Vrekoussis, M., Bloss, W. J., Clapp, L. J., Kortner, M., Dorn, H.-P., Monks, P. S., Platt, U., Plass-Dülmer, C., Mihalopoulos, N., Heard, D. E., Clemitshaw, K. C., Meixner, F. X., Prevot, A. S. H., and Schmitt, R.: Photolysis frequency measurement techniques: results of a comparison within the ACCENT project, Atmos. Chem. Phys., 8, 5373–5391, doi:10.5194/acp-8-5373-2008, 2008.

Boy, M. and Kulmala, M.: The part of the solar spectrum with the highest influence on the formation of SOA in the continental boundary layer, Atmos. Chem. Phys., 2, 375–386, doi:10.5194/acp-2-375-2002, 2002.

Boy, M., Sogachev, A., Lauros, J., Zhou, L., Guenther, A., and Smolander, S.: SOSA – a new model to simulate the concentrations of organic vapours and sulphuric acid inside the ABL – Part 1: Model description and initial evaluation, Atmos. Chem. Phys., 11, 43–51, doi:10.5194/acp-11-43-2011, 2011.

Boy, M., Mogensen, D., Smolander, S., Zhou, L., Nieminen, T., Paasonen, P., Plass-Dülmer, C., Sipilä, M., Petäjä, T., Mauldin, L., Berresheim, H., and Kulmala, M.: Oxidation of SO_2 by stabilized Criegee intermediate (sCI) radicals as a crucial source for atmospheric sulfuric acid concentrations, Atmos. Chem. Phys., 13, 3865–3879, doi:10.5194/acp-13-3865-2013, 2013.

Brown, S. S., Ryerson, T. B., Wollny, A. G., Brock, C. A., Peltier, R., Sullivan, A. P., Weber, R. J., Dube, W. P., Trainer, M., Meagher, J. F., Fehsenfeld, F. C., and Ravishankara, A. R.: Variability in nocturnal nitrogen oxide processing and its role in regional air quality, Science, 311, 67–70, 2006.

Brown, S. S., Dubé, W. P., Peischl, J., Ryerson, T. B., Atlas, E., Warneke, C., de Gouw, J. A., te Lintel Hekkert, S., Brock, C. A., Flocke, F., Trainer, M., Parrish, D. D., Feshenfeld, F. C., and Ravishankara, A. R.: Budgets for nocturnal VOC oxidation by nitrate radicals aloft during the 2006 Texas Air Quality Study, J. Geophys. Res., 116, D24305, doi:10.1029/2011JD016544, 2011.

Browne, E. C. and Cohen, R. C.: Effects of biogenic nitrate chemistry on the NO_x lifetime in remote continental regions, Atmos. Chem. Phys., 12, 11917–11932, doi:10.5194/acp-12-11917-2012, 2012.

Browne, E. C., Wooldridge, P. J., Min, K.-E., and Cohen, R. C.: On the role of monoterpene chemistry in the remote continental boundary layer, Atmos. Chem. Phys., 14, 1225–1238, doi:10.5194/acp-14-1225-2014, 2014.

Chang, W. L., Bhave, P. V., Brown, S. S., Riemer, N., Stutz, J., and Dabdub, D.: Heterogeneous atmosperic chemistry, ambient measurements and model calculatuons of N_2O_5: a review, Aerosol Sci. Tech., 45, 655–685, 2011.

Crowley, J. N., Ammann, M., Cox, R. A., Hynes, R. G., Jenkin, M. E., Mellouki, A., Rossi, M. J., Troe, J., and Wallington, T. J.: Evaluated kinetic and photochemical data for atmospheric chemistry: Volume V – heterogeneous reactions on solid substrates, Atmos. Chem. Phys., 10, 9059–9223, doi:10.5194/acp-10-9059-2010, 2010a.

Crowley, J. N., Schuster, G., Pouvesle, N., Parchatka, U., Fischer, H., Bonn, B., Bingemer, H., and Lelieveld, J.: Nocturnal nitrogen oxides at a rural mountain-site in south-western Germany, Atmos. Chem. Phys., 10, 2795–2812, doi:10.5194/acp-10-2795-2010, 2010b.

Damian, V., Sandu, A., Damian, M., Potra, F., and Carmichael, G. R.: The kinetic preprocessor KPP – a software environment for solving chemical kinetics, Comput. Chem. Eng., 26, 1567–1579, 2002.

Dee, D. P., Uppala, S. M., Simmons, A. J., Berrisford, P., Poli, P., Kobayashi, S., Andrae, U., Balmaseda, M. A., Balsamo, G., Bauer, P., Bechtold, P., Beljaars, A. C. M., van de Berg, L., Bidlot, J., Bormann, N., Delsol, C., Dragani, R., Fuentes, M., Geer, A. J., Haimberger, L., Healy, S. B., Hersbach, H., Hólm, E. V., Isaksen, L., Kållberg, P., Köhler, M., Matricardi, M., McNally, A. P., Monge-Sanz, B. M., Morcrette, J.-J., Park, B.-K., Peubey, C., de Rosnay, P., Tavolato, C., Thépaut, J.-N., and Vitart, F.: The ERA-Interim reanalysis: configuration and performance of the data assimilation system, Q. J. Roy. Meteor. Soc., 137,553–597, 2011.

Di Carlo, P., Brune, W. H., Martinez, M., Harder, H., Lesher, R., Ren, X., Thornberry, T., Carroll, M. A., Young, V., Shepson, P. B., Riemer, D., Apel, E., and Campbell, C.: Missing OH reactivity in a forest: Evidence for unknown reactive biogenic VOCs, Science, 304, 722–725, 2004.

Ehn, M., Thornton, J. A., Kleist, E., Sipilä, M., Junninen, H., Pullinen, I., Springer, M., Rubach, F., Tillmann, R., Lee, B., Lopez-Hilfiker, F., Andres, S., Acir, I.-H., Rissanen, M., Jokinen, T., Schobesberger, S., Kangasluoma, J., Kontkanen, J., Nieminen, T., Kurtén, T., Nielsen, L. B., Jorgensen, S., Kjaergaard, H. G., Canagaratna, M., Dal Maso, M., Berndt, T., Petaja, T., Wahner, A., Kerminen, V.-M., Kulmala, M., Worsnop, D. R., Wildt, J., and Mentel, T. F.: A large source of low-volatility secondary organic aerosol, Nature, 506, 476–479, 2014.

Foken, T.: The energy balance closure problem: an overview, Ecol. Appl., 18, 1351–1367, 2008.

Geyer, A., Ackermann, R., Dubois, R., Lohrmann, B., Muller, T., and Platt, U.: Long–term observation of nitrate radicals in the continental boundary layer near Berlin, Atmos. Environ., 35, 3619–3631, 2001.

Guenther, A.: Biological and chemical diversity of biogenic volatile organic emissions into the atmosphere, ISRN Atmospheric Sciences, 2013, 786290, doi:10.1155/2013/786290, 2013.

Guenther, A., Karl, T., Harley, P., Wiedinmyer, C., Palmer, P. I., and Geron, C.: Estimates of global terrestrial isoprene emissions using MEGAN (Model of Emissions of Gases and Aerosols from Nature), Atmos. Chem. Phys., 6, 3181–3210, doi:10.5194/acp-6-3181-2006, 2006.

Haapanala, S., Rinne, J., Hakola, H., Hellén, H., Laakso, L., Lihavainen, H., Janson, R., O'Dowd, C., and Kulmala, M.: Boundary layer concentrations and landscape scale emissions of volatile organic compounds in early spring, Atmos. Chem. Phys., 7, 1869–1878, doi:10.5194/acp-7-1869-2007, 2007.

Hakola, H., Tarvainen, V., Laurila, T., Hiltunen, V., Hellén, H., and Keronen, P.: Seasonal variation of VOC concentrations above a boreal coniferous forest, Atmos. Environ., 37, 1623–1634, 2003.

Hakola, H., Tarvainen, V., Bäck, J., Ranta, H., Bonn, B., Rinne, J., and Kulmala, M.: Seasonal variation of mono- and sesquiterpene emission rates of Scots pine, Biogeosciences, 3, 93–101, doi:10.5194/bg-3-93-2006, 2006.

Hari, P. and Kulmala, M.: Station for measuring ecosystem–atmosphere relations (SMEAR II), Boreal Environ. Res., 10, 315–322, 2005.

Hens, K., Novelli, A., Martinez, M., Auld, J., Axinte, R., Bohn, B., Fischer, H., Keronen, P., Kubistin, D., Nölscher, A. C., Oswald, R., Paasonen, P., Petäjä, T., Regelin, E., Sander, R., Sinha, V., Sipilä, M., Taraborrelli, D., Tatum Ernest, C., Williams, J., Lelieveld, J., and Harder, H.: Observation and modelling of HO_x radicals in a boreal forest, Atmos. Chem. Phys., 14, 8723–8747, doi:10.5194/acp-14-8723-2014, 2014.

Hosaynali Beygi, Z., Fischer, H., Harder, H. D., Martinez, M., Sander, R., Williams, J., Brookes, D. M., Monks, P. S., and Lelieveld, J.: Oxidation photochemistry in the Southern Atlantic

boundary layer: unexpected deviations of photochemical steady state, Atmos. Chem. Phys., 11, 8497–8513, doi:10.5194/acp-11-8497-2011, 2011.

Ilvesniemi, H., Levula, J., Ojansuu, R., Kolari, P., Kulmala, L., Pumpanen, J., Launiainen, S., Vesala, T., and Nikinmaa, E.: Long-term measurements of the carbon balance of a boreal Scots pine dominated forest ecosystem, Boreal Environ. Res., 14, 731–753, 2009.

IUPAC: Task Group on Atmospheric Chemical Kinetic Data Evaluation (Ammann, M., Cox, R. A., Crowley, J. N., Jenkin, M. E., Mellouki, A., Rossi, M. J., Troe, J., and Wallington, T. J.), available at: http://iupac.pole-ether.fr/index.html (last access: 14 April 2015), 2014.

Jacob, D. J.: Introduction to Atmospheric Chemistry, Princeton University Press, 1999.

Jenkin, M. E., Saunders, S. M., and Pilling, M. J.: The tropospheric degradation of volatile organic compounds: a protocol for mechanism development, Atmos. Environ., 12, 5275–5308, 2012.

Jenkin, M. E., Wyche, K. P., Evans, C. J., Carr, T., Monks, P. S., Alfarra, M. R., Barley, M. H., McFiggans, G. B., Young, J. C., and Rickard, A. R.: Development and chamber evaluation of the MCM v3.2 degradation scheme for β-caryophyllene, Atmos. Chem. Phys., 12, 5275–5308, doi:10.5194/acp-12-5275-2012, 2012.

Kazadzis, S., Bais, A. F., Balis, D., Zerefos, C. S., and Blumthaler, M.: Retrieval of downwelling UV actinic flux density spectra from spectral measurements of global and direct solar UV irradiance, J. Geophys. Res., 105, 4857–4864, 2000.

Kazadzis, S., Topaloglou, C., Bais, A. F., Blumthaler, M., Balis, D., Kazantzidis, A., and Schallhart, B.: Actinic flux and O^1D photolysis frequencies retrieved from spectral measurements of irradiance at Thessaloniki, Greece, Atmos. Chem. Phys., 4, 2215–2226, doi:10.5194/acp-4-2215-2004, 2004.

Kovacs, T. A., Brune, W. H., Harder, H., Martinez, M., Simpas, J. B., Frost, G. J., Williams, E., Jobson, T., Stroud, C., Young, V., Friede, A., and Werte, B.: Direct measurements of urban OH reactivity during Nashville SOS in summer 1999, J. Environ. Monitor., 5, 68–74, 2003.

Kulmala, M., Hämeri, K., Aalto, P. P., Mäkelä, J. M., Pirjola, L., Nilsson, E. D., Buzorius, G., Rannik, Ü., Dal Maso, M., Seidl, W., Hoffman, T., Janson, R., Hansson, H.-C., Viisanen, Y., Laaksonen, A., and O'Dowd, C. D.: Overview of the international project on biogenic aerosol formation in the boreal forest (BIOFOR), Tellus B, 53, 324–343, 2001a.

Kulmala, M., Dal Maso, M., Mäkelä, J. M., Pirjola, L., Väkevä, M., Aalto, P., Miikkulainen, P., Hämeri, K., and O'Dowd, C. D.: On the formation, growth and composition of nucleation mode particles, Tellus B, 53, 479–490, 2001b.

Kylling, A., Webb, A. R., Bais, A. F., Blumthaler, M., Schmitt, R., Thiel, S., Kazantzidis, A., Kift, R., Misslbeck, M., Schallhart, B., Schreder, J., Topaloglou, C., Kazadzis, S., and Rimmer, J.: Actinic flux determination from measurements of irradiance, J. Geophys. Res.-Atmos., 108, 4506–4515, 2003.

Lelieveld, J., Butler, T. M., Crowley, J. N., Dillon, T. J., Fischer, H., Ganzeveld, L., Harder, H., Lawrence, M. G., Martinez, M., Taraborrelli, D., and Williams, J.: Atmospheric oxidation capacity sustained by a tropical forest, Nature, 452, 737–740, 2008.

Levy II, H.: Normal atmosphere: large radical and formaldehyde concentrations predicted, Science, 173, 141–143, 1971.

Lou, S., Holland, F., Rohrer, F., Lu, K., Bohn, B., Brauers, T., Chang, C.C., Fuchs, H., Häseler, R., Kita, K., Kondo, Y., Li, X., Shao, M., Zeng, L., Wahner, A., Zhang, Y., Wang, W., and Hofzumahaus, A.: Atmospheric OH reactivities in the Pearl River Delta – China in summer 2006: measurement and model results, Atmos. Chem. Phys., 10, 11243–11260, doi:10.5194/acp-10-11243-2010, 2010.

Madronich, S.: Photodissociation in the atmosphere: 1. Actinic flux and the effects of ground reflections and clouds, J. Geophys. Res., 92, 9740–9752, 1987.

Makkonen, R., Asmi, A., Kerminen, V.-M., Boy, M., Arneth, A., Guenther, A., and Kulmala, M.: BVOC-aerosol-climate interactions in the global aerosol-climate model ECHAM5.5-HAM2, Atmos. Chem. Phys., 12, 10077–10096, doi:10.5194/acp-12-10077-2012, 2012.

Mao, J., Ren, X., Zhang, L., Van Duin, D. M., Cohen, R. C., Park, J.-H., Goldstein, A. H., Paulot, F., Beaver, M. R., Crounse, J. D., Wennberg, P. O., DiGangi, J. P., Henry, S. B., Keutsch, F. N., Park, C., Schade, G. W., Wolfe, G. M., Thornton, J. A., and Brune, W. H.: Insights into hydroxyl measurements and atmospheric oxidation in a California forest, Atmos. Chem. Phys., 12, 8009–8020, doi:10.5194/acp-12-8009-2012, 2012.

Markkanen, T., Rannik, Ü., Keronen, P., Suni, T., and Vesala, T.: Eddy covariance fluxes over a boreal Scots pine forest, Boreal Environ. Res., 6, 65–78, 2001.

Matsumoto, J.: Measuring Biogenic Volatile Organic Compounds (BVOCs) from vegetation in terms of ozone reactivity, Aerosol Air Qual. Res., 14, 197–206, 2014.

Mauldin III, R. L., Berndt, T., Sipilä, M., Paasonen, P., Petäjä, T., Kim, S., Kurtén, T., Stratmann, F., Kerminen, V.-M., and Kulmala, M.: A new atmospherically relevant oxidant, Nature, 488, 193–196, 2012.

Mogensen, D., Smolander, S., Sogachev, A., Zhou, L., Sinha, V., Guenther, A., Williams, J., Nieminen, T., Kajos, M. K., Rinne, J., Kulmala, M., and Boy, M.: Modelling atmospheric OH-reactivity in a boreal forest ecosystem, Atmos. Chem. Phys., 11, 9709–9719, doi:10.5194/acp-11-9709-2011, 2011.

Mogensen, D., Aaltonen, H., Aalto, J., Bäck, J., Gierens, R., Guenther, A., Smolander, S., Rantala, P., Song, W., Kulmala, M., and Boy, M.: Implementation of forest floor terpenoid emission and model validation by BVOCs, Biogeosciences Discuss., in preparation, 2015.

Mount, G. H. and Eisele, F. L.: An intercomparison of tropospheric OH measurements at Fritz Peak Observatory, Colerado, Science, 256, 1187–1190, 1992.

Nölscher, A. C., Williams, J., Sinha, V., Custer, T., Song, W., Johnson, A. M., Axinte, R., Bozem, H., Fischer, H., Pouvesle, N., Phillips, G., Crowley, J. N., Rantala, P., Rinne, J., Kulmala, M., Gonzales, D., Valverde-Canossa, J., Vogel, A., Hoffmann, T., Ouwersloot, H. G., Vilà-Guerau de Arellano, J., and Lelieveld, J.: Summertime total OH reactivity measurements from boreal forest during HUMPPA-COPEC 2010, Atmos. Chem. Phys., 12, 8257–8270, doi:10.5194/acp-12-8257-2012, 2012a.

Nölscher, A. C., Sinha, V., Bockisch, S., Klüpfel, T., and Williams, J.: Total OH reactivity measurements using a new fast Gas Chromatographic Photo-Ionization Detector (GC-PID), Atmos. Meas. Tech., 5, 2981–2992, doi:10.5194/amt-5-2981-2012, 2012b.

Novelli, A., Hens, K., Tatum Ernest, C., Kubistin, D., Regelin, E., Elste, T., Plass-Dülmer, C., Martinez, M., Lelieveld, J.,

and Harder, H.: Characterisation of an inlet pre-injector laser-induced fluorescence instrument for the measurement of atmospheric hydroxyl radicals, Atmos. Meas. Tech., 7, 3413–3430, doi:10.5194/amt-7-3413-2014, 2014a.

Novelli, A., Vereecken, L. Lelieveld, J., and Harder, H.: Direct observation of OH formation from stabilised Criegee intermediates, Phys. Chem. Chem. Phys., 16, 19941–19951, 2014b.

Ouwersloot, H. G., Vilà-Guerau de Arellano, J., Nölscher, A. C., Krol, M. C., Ganzeveld, L. N., Breitenberger, C., Mammarella, I., Williams, J., and Lelieveld, J.: Characterization of a boreal convective boundary layer and its impact on atmospheric chemistry during HUMPPA-COPEC-2010, Atmos. Chem. Phys., 12, 9335–9353, doi:10.5194/acp-12-9335-2012, 2012.

Palmroth, S. and Hari, P.: Evaluation of the importance of acclimation of needle structure, photosynthesis, and respiration to available photosynthetically active radiation in a Scots pine canopy, Can. J. Forest Res., 31, 1235–1243, 2001.

Park, J.-H., Guenther, A., and Helmig, D.: Ozone reactivity of biogenic volatile organic compound (BVOC) emissions during the Southeast Oxidant and Aerosol Study (SOAS), AGU Fall Meeting, San Francisco, 9–13 December, Abstract A13A-0172, 2013.

Peräkylä, O., Vogt, M., Tikkanen, O.-P., Laurila, T., Kajos, M. K., Rantala, P. A., Patokoski, J., Aalto, J., Yli-Juuti, T., Ehn, M., Sipilä, M., Paasonen, P., Rissanen, M., Nieminen, T., Taipale, R., Keronen, P., Lappalainen, H. K., Ruuskanen, T. M., Rinne, J., Kerminen, V.-M., Kulmala, M., Bäck, J., and Petäjä, T.: Monoterpenes' oxidation capacity and rate over a boreal forest: temporal variation and connection to growth of newly formed particles, Boreal Environ. Res., 19, 293–310, 2014.

Radhakrishnan, K. and Hindmarsh, A. C.: Description and use of LSODE, the Livermore Solver for Ordinary Differential Equations, LLNL report UCRL-ID-113855, December 1993.

Rannik, Ü., Altimir, N., Mammarella, I., Bäck, J., Rinne, J., Ruuskanen, T. M., Hari, P., Vesala, T., and Kulmala, M.: Ozone deposition into a boreal forest over a decade of observations: evaluating deposition partitioning and driving variables, Atmos. Chem. Phys., 12, 12165–12182, doi:10.5194/acp-12-12165-2012, 2012.

Ren, X. R., Harder, H., Martinez, M., Lesher, R. L., Oliger, A., Shirley, Y., Adams, J., Simpas, J. B., and Brune, W. H.: HO_X concentrations and OH reactivity observations in New York city during PMTACS-NY2001, Atmos. Environ., 37, 3627–3637, 2003.

Rinne, J., Markkanen, T., Ruuskanen, T. M., Petäjä, T., Keronen, P., Tang, M. J., Crowley, J. N., Rannik, Ü., and Vesala, T.: Effect of chemical degradation on fluxes of reactive compounds – a study with a stochastic Lagrangian transport model, Atmos. Chem. Phys., 12, 4843–4854, doi:10.5194/acp-12-4843-2012, 2012.

Rosman, K., Shimmo, M., Karlsson, A., Hansson, H.-C. Keronen, P., Allen, A., and Hoenninger, G.: Laboratory and field investigations of a new and simple design for the parallel plate denuder, Atmos. Environ., 35, 5301–5310, 2001.

Saunders, S. M., Jenkin, M. E., Derwent, R. G., and Pilling, M. J.: Protocol for the development of the Master Chemical Mechanism, MCM v3 (Part A): tropospheric degradation of non-aromatic volatile organic compounds, Atmos. Chem. Phys., 3, 161–180, doi:10.5194/acp-3-161-2003, 2003.

Schuster, G., Labazan, I., and Crowley, J. N.: A cavity ring down/cavity enhanced absorption device for measurement of ambient NO_3 and N_2O_5, Atmos. Meas. Tech., 2, 1–13, doi:10.5194/amt-2-1-2009, 2009.

Simpson, D., Winiwarter, W., Borjesson, G., Cinderby, S., Ferreiro, A., Guenther, A., Hewitt, C. N., Janson, R., Khalil, M. A. K., Owen, S., Pierce, T. E., Puxbaum, H., Shearer, M., Skiba, U., Steinbrecher, R., Tarrason, L., and Oquist, M. G.: Inventorying emissions from nature in Europe, J. Geophys. Res., 104, 8113–8152, 1999.

Simpson, I. J., Thurtell, G. W., Neumann, H. H., Den Hartog, G., and Edwards, G. C.: The validity of similarity theory in the roughness sublayer above forests, Bound.-Lay. Meteorol., 87, 69–99, 1998.

Sinha, V., Williams, J., Crowley, J. N., and Lelieveld, J.: The Comparative Reactivity Method – a new tool to measure total OH Reactivity in ambient air, Atmos. Chem. Phys., 8, 2213–2227, doi:10.5194/acp-8-2213-2008, 2008.

Sinha, V., Williams, J., Lelieveld, J., Ruuskanen, T. M., Kajos, M. K., Patokoski, J., Hellén, H., Hakola, H., Mogensen, D., Boy, M., Rinne, J., and Kulmala, M.: OH reactivity measurements within a boreal forest: evidence for unknown reactive emissions, Environ. Sci. Technol., 44, 6614–6620, 2010.

Smolander, S., He, Q., Mogensen, D., Zhou, L., Bäck, J., Ruuskanen, T., Noe, S., Guenther, A., Aaltonen, H., Kulmala, M., and Boy, M.: Comparing three vegetation monoterpene emission models to measured gas concentrations with a model of meteorology, air chemistry and chemical transport, Biogeosciences, 11, 5425–5443, doi:10.5194/bg-11-5425-2014, 2014.

Sogachev, A.: A note on two-equation closure modelling of canopy flow, Bound.-Lay. Meteorol., 130, 423–435, 2009.

Sogachev, A., Menzhulin, G. V., Heimann, M., and Lloyd, M. H.: A simple three-dimensional canopy – planetary boundary layer simulation model for scalar concentrations and fluxes, Tellus B, 54, 784–819, 2002.

Sogachev, A., Kelly, M., and Leclerc, M. Y.: Consistent two-equation closure modeling for atmospheric research: buoyancy and vegetation implementations, Bound.-Lay. Meteorol., 145, 307–327, 2012.

Stone, D., Whalley, L. K., and Heard, D. E.: Tropospheric OH and HO_2 radicals: field measurements and model comparisons, Chem. Soc. Rev., 41, 6348–6404, 2012.

Stull, R. B.: An Introduction to Boundary Layer Meteorology, Springer, Vol. 13, 1988.

Tarvainen, V., Hakola, H., Hellén, H., Bäck, J., Hari, P., and Kulmala, M.: Temperature and light dependence of the VOC emissions of Scots pine, Atmos. Chem. Phys., 5, 989–998, doi:10.5194/acp-5-989-2005, 2005.

Vesala, T., Haataja, J., Aalto, P., Altimir, N., Buzorius, G., Garam, E., Hämeri, K., Ilvesniemi, H., Jokinen, V., Keronen, P., Lahti, T., Markkanen, T., Mäkelä, J. M., Nikinmaa, E., Palmroth, S., Palva, L., Pohja, T., Pumpanen, J., Rannik, Ü., Siivola, E., Ylitalo, H., Hari, P., and Kulmala, M.: Long-term field measurements of atmospheric–surface interactions in boreal forest combining forest ecology, micrometeorology, aerosol physics and atmospheric chemistry, Trends in Heat, Mass and Momentum Transfer, 4, 17–35, 1998.

Wang, C. C. and Davis, L. I.: Measurement of hydroxyl concentrations in air using a tunable uv laser beam, J. Phys. Rev. Lett., 32, 349–352, 1974.

Webb, A. R., Kift, R., Thiel, S., and Blumthaler, M.: An empirical method for the conversion of spectral UV irradiance measurements to actinic flux data, Atmos. Environ., 36, 4397–4404, 2002.

Welz, O., Savee, J. D., Osborn, D. L., Vasu, S. S., Percival, C. J., Shallcross, D. E., and Taatjes, C. A.: Direct kinetic measurements of Criegee Intermediate (CH_2OO) formed by reaction of CH_2I with O_2, Science, 335, 204–207, 2012.

Williams, J., Crowley, J., Fischer, H., Harder, H., Martinez, M., Petäjä, T., Rinne, J., Bäck, J., Boy, M., Dal Maso, M., Hakala, J., Kajos, M., Keronen, P., Rantala, P., Aalto, J., Aaltonen, H., Paatero, J., Vesala, T., Hakola, H., Levula, J., Pohja, T., Herrmann, F., Auld, J., Mesarchaki, E., Song, W., Yassaa, N., Nölscher, A., Johnson, A. M., Custer, T., Sinha, V., Thieser, J., Pouvesle, N., Taraborrelli, D., Tang, M. J., Bozem, H., Hosaynali-Beygi, Z., Axinte, R., Oswald, R., Novelli, A., Kubistin, D., Hens, K., Javed, U., Trawny, K., Breitenberger, C., Hidalgo, P. J., Ebben, C. J., Geiger, F. M., Corrigan, A. L., Russell, L. M., Ouwersloot, H. G., Vilà-Guerau de Arellano, J., Ganzeveld, L., Vogel, A., Beck, M., Bayerle, A., Kampf, C. J., Bertelmann, M., Köllner, F., Hoffmann, T., Valverde, J., González, D., Riekkola, M.-L., Kulmala, M., and Lelieveld, J.: The summertime Boreal forest field measurement intensive (HUMPPA-COPEC-2010): an overview of meteorological and chemical influences, Atmos. Chem. Phys., 11, 10599–10618, doi:10.5194/acp-11-10599-2011, 2011.

Willmott, C. J.: On the validation of models, Phys. Geogr., 2, 184–194, 1981.

Wolfe, G. M., Thornton, J. A., McKay, M., and Goldstein, A. H.: Forest-atmosphere exchange of ozone: sensitivity to very reactive biogenic VOC emissions and implications for in-canopy photochemistry, Atmos. Chem. Phys., 11, 7875–7891, doi:10.5194/acp-11-7875-2011, 2011.

Zhou, L., Nieminen, T., Mogensen, D., Smolander, S., Rusanen, A., Kulmala, M., and Boy, M.: SOSAA – a new model to simulate the concentrations of organic vapours, sulphuric acid and aerosols inside the ABL – Part 2: Aerosol dynamics and one case study at a boreal forest site, Boreal Environ. Res., 19, 237–256, 2014.

Zilitinkevich, S. and Mironov, D. V.: A multi-limit formulation for the equilibrium depth of a stably stratified boundary layer, Bound.-Lay. Meteorol., 81, 325–351, 1996.